AD_____

Award Number: DAMD17-97-1-7300

TITLE: Computer Simulation of X-Ray Capillary Optice for Digital Mammography

PRINCIPAL INVESTIGATOR: Cari
Carolyn MacDonald, Ph.D.

CONTRACTING ORGANIZATION: State University of New York
Albany, New York 12222

REPORT DATE: September 2000

TYPE OF REPORT: Final

PREPARED FOR: U.S. Army Medical Research and Materiel Command
Fort Detrick, Maryland 21702-5012

REPORT DOCUMENTATION PAGE

OMB No. 074-0188

1. AGENCY USE ONLY (Leave blank)	2. REPORT DATE	3. REPORT TYPE AND DATES COVERED
	September 2000	Final (1 Sep 97 - 31 Aug 00)

4. TITLE AND SUBTITLE
Computer Simulation of X-Ray Capillary Optice for Digital Mammography

5. FUNDING NUMBERS
DAMD17-97-1-7300

6. AUTHOR(S)
Cari
Carolyn MacDonald, Ph.D.

7. PERFORMING ORGANIZATION NAME(S) AND ADDRESS(ES)
State University of New York
Albany, New York 12222

E-MAIL:
cx1122@cnsvax.albany.edu

8. PERFORMING ORGANIZATION REPORT NUMBER

9. SPONSORING / MONITORING AGENCY NAME(S) AND ADDRESS(ES)
U.S. Army Medical Research and Materiel Command
Fort Detrick, Maryland 21702-5012

10. SPONSORING / MONITORING AGENCY REPORT NUMBER

11. SUPPLEMENTARY NOTES

12a. DISTRIBUTION / AVAILABILITY STATEMENT
Approved for public release; distribution unlimited

12b. DISTRIBUTION CODE

13. ABSTRACT ***(Maximum 200 Words)***

Polycapillary x-ray optics, arrays of hollow capillary tubes used to guide x rays by total reflectance, are now being used in increasing numbers of applications, such as materials analysis, microelectronics manufacturing, x-ray astronomy and medical imaging. Because each optic contains hundreds of thousands of precisely shaped and located hollow channels, it is desirable to assess the feasibility of a variety of capillary geometries for a new application without physically constructing the optic. This assessment requires increasingly sophisticated modeling capability as new applications with more stringent requirements are developed. Previous analysis has shown that high-energy applications such as hard x-ray astronomy and medical imaging are particularly sensitive to optic profile errors such as channel waviness. A more physical model for surface waviness has been developed and included in optics simulations. The results are compared to measured data and to the results of other numerical simulation programs.

Directed digital mammography can avail itself the advantages of digital processing, including tolerance to under- and over-exposure and image enhancement. In addition, a new technology, polycapillary optics, has been shown to produce clearer image by increasing contrast and resolution. Capillary optics, consisting a array of hollow glass tubes, is a relatively new technology for controlling x-ray beams. Thousands of individual capillary fiber can be strung together to form a multifiber optic. These arrays of curve polycapillary fiber can be used to focus, collimate, and filter x-ray radiation. A number of borrosilicate glass capillary fibers have beeen measured and simulated in the energy range 10-80 keV. The result shown potential for mammography applications, with transmission of 70 % at 20 keV. A multifiber optics constructed of several thousand of these fiber was 3 cm X 3 cm on the parallel end, 2.9 cm x 2.9 cm on the focusing end, and ha a focal length about 200 cm. This optic, characterized in the collimating mode, had quite high transmission of about 45 % at 20 keV with uniform output across the field. The output divergence was low, 1.2 mrad at 17.5 keV, which indicates very good alignment. The optic was also used with a parallel beam input, in focusing mode, to measure image demagnification. In addition to the magnification, images taken 20 cm behind the optic demonstrated a contrast enhancement of a factor of 1.4 at 20 keV, due to rejection of Compton scattering.

14. SUBJECT TERMS	15. NUMBER OF PAGES
Breast Cancer	42
	16. PRICE CODE

17. SECURITY CLASSIFICATION OF REPORT	18. SECURITY CLASSIFICATION OF THIS PAGE	19. SECURITY CLASSIFICATION OF ABSTRACT	20. LIMITATION OF ABSTRACT
Unclassified	Unclassified	Unclassified	Unlimited

Table of Contents

1. Introduction

1.A Background:

Each year about 186,000 women contract breast cancer, of whom 46,000 will die of it. Breast cancer is the leading cause of cancer deaths amongst American women aged 35 to 50 and also has the highest cancer mortality rate for younger women. Mammography is most widely used modality for early detection of breast cancer. The detection of tiny carcinomas and low contrast tissue is essential for mammography to reduce the mortality rate[1, 2]. It has been shown that about 20% of detectable cancers are overlooked or misdiagnosed on first detection. We obviously need a major improvement in the quality of mammograghic imaging. Using an innovative new technology x-ray optics to improve system resolution, enhance contrast and reduce dosage will increase the effectiveness of this proven screening modality, with a direct impact on mortality.

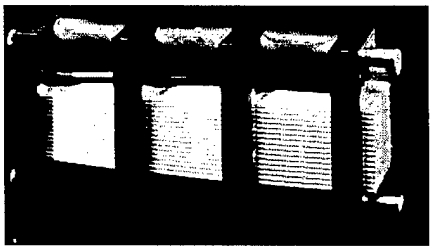

Figure 1 Complete optic constructed by configuring fibers through metal grids.

1.B Benefits of digital mammography

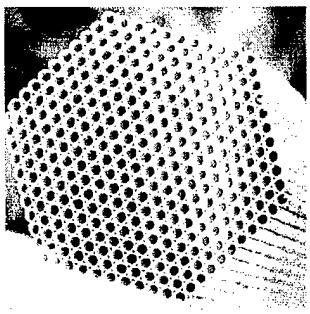

Figure 2 Cross section of polycapillary fiber. 0.5 mm in diameter. SEM photo.

Conventional film screen mammography suffers from limited dynamic range and film granularity, which can reduce the sensitivity to detect microcalcifications. The primary theoretical limitations of mammography are the system resolution, which determines the minimum size of the detectable malignancy, and the need to expose the patient to ionizing radiation. Using innovative new technology -- polycapillary optics -- to improve system resolution and reduce required dose will increase the effectiveness of this proven screening modality, with a direct and immediate impact on mortality. By matching polycapillary optics to digital detectors, we can develop direct digital mammographic systems which can avail themselves of the advantages of digital processing, including improved image contrast and resolution at reduced radiation dose. In practice, mammographic imaging is often limited by quality assurance issues, which can also be favorably addressed by digital processing. Digital detection can provide high dynamic range which, in addition to improving contrast, greatly increases the tolerance of the final image to under or over exposure. Digital images can be enhanced and are amenable to computer-aided diagnosis. Finally, digital images can also be transported quickly for skilled consultations.

1.C What capillary x-ray optics can do

Capillary optics, consisting of arrays of hollow glass tubes, is a relatively new technology for controlling X-ray beams. X-rays incident on the interior of the glass tubes at small angles are guided down the tubes by total external reflection. Arrays of curved/tapered capillaries can be used to focus, collimate and filter X-ray radiation[3,4,5,6,7]. Such arrays are manufactured by stringing hollow glass polycapillaries through metal grids (as in Figure 1) or as a monolithic optic.

The use of Kumakhov capillary optics in place of conventional scatter reduction grids in a mammographic system has significant potential to provide improved resolution, increased contrast enhancement and reduced dose in mammographic imaging. The optics can also be used to mate the radiographic image with a digital detector by appropriate choice of demagnification and separation to discrete chips. In addition, a pre-patient optic could be employed to increase the available intensity in a fan beam relative to simple slot collimating.

The fibers in this research varied from 0.3 mm to 4 mm in outer diameter, with channel sizes (the diameters of the holes within the fibers) ranging from 4 to 22 μm, as shown in Table 1 in section 2.E. Open area in the table refers to the fraction of the front face of the fiber which is open channels, as opposed to glass walls. No fiber can have a transmission that is greater than the open area.

X-ray beams can be bent, focused or collimated by a carefully curved polycapillary array. X-ray photon energies are much larger than the plasma frequencies of glasses, which are tens of electron volts. In this regime, the real part of the index of refraction of glass can be simply approximated by

$$n^2 = \frac{\varepsilon}{\varepsilon_o} \approx 1 - \frac{\omega_p^2}{\omega^2} \quad (1)$$

where n is the index of refraction, ε is the dielectric constant of the glass, ω is the photon frequency, ω_p is the plasma frequency of the material, and ε_0 is the dielectric constant for vacuum.

The plasma frequency ω_p for glass is small compared to the photon frequency, so that n is slightly less than unity. Therefore, x rays traveling in vacuum or air can be totally externally reflected from smooth glass surfaces. The maximum angle between the x-ray beam and glass surface for total reflection, θ_c, is approximately

$$\theta_c = \frac{30}{E} \text{ mrad}, \quad (2)$$

where E is the photon energy in keV. The higher the energy of photon, the smaller is the critical angle. For this reason, profile errors that change the angle of incidence are more detrimental at high energies.

1.D Numerical simulations

To evaluate the experimental performance of capillaries and optics, and to design capillary optics, it is necessary to be able to predict theoretical behavior for complex geometries. Extensive modeling programs describing the propagation of x-rays along capillaries and optics are being developed. These modeling programs provide essential information on the transmission efficiency and divergence of capillary optics, and are being used to simulate the performance of the optics by obtaining the following outputs: transmission efficiency, exit divergence, output uniformity, and transmission as a function of entrance angle.

The models for these simulation programs are based on Monte Carlo simulations of simple geometrical optics. The simulations randomly generate millions of x-ray photons from a particular location and solid angle, and then trace them through the optics using reflection theory and classic mechanics. The necessary confidence in the simulations is being built by comparing the results of the modeling program with experimental data.

For single fibers, the computational speed is greatly enhanced by a reduction to two dimensions by projecting the trajectory onto the local fiber cross-section.[8] Reflections are computed from standard tables.[9]

1.E Purpose

The purpose of this project is to contribute to an ongoing effort to use the new innovative technologies in X-ray optics to develop a digital mammographic imaging system with high resolution and contrast by extending the capabilities of the computer simulation. Enhanced computer simulations are critical because manufacturing large polycapillary optics is difficult, expensive and time-consuming, and simulation is a good design tool to predict the performance of the optics and make it clear how all the different parameters work together and impact the resultant transmission, resolution and contrast.

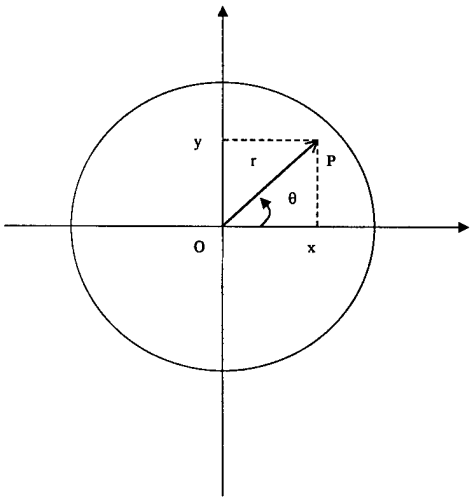

Figure 3. The generation of a random point (of a photon) in a circle.

1.F Technical objectives

The specific aims of this traineeship are:

- to simulate and measure trial optic setups, to compare the simulated results with experimental data and to determine the best design for building the best direct digital mammographic system;
- to further the author's knowledge about the mammographic systems and to promote a future career in this field.

2. Body: Methods and Results

2.A Introduction to profile and surface defect corrections

Real glass surfaces are not perfect. In addition to absorption, there is roughness, which has short wavelengths, of the order of microns or less, waviness, which has longer wavelength, and bending, which has wavelength longer than the length of the capillary. Bending is described by the radius of curvature of the fiber, R in Table 1. Waviness results in the channel wall being tilted with respect to the axis of the fiber, and therefore changes the angle of incidence. It is described in terms of a distribution of tilt angles. Surface roughness produces both diffuse scattering, for which the reflected angle can be either larger or smaller than the corresponding incident angle, and transmission into the glass. The roughness correction[10] used in previous simulations[11] is described in terms of a roughness height, z and a correlation length, s.

2.B Statement of Work

To provide a framework for assessing the results of the project, the original statement of work for the full three-year project is reproduced below.

Proposed Statement Of Work

Task 1 Developing and testing the simulation software. (months 1-18)

Task 2: Perform experiment and geometric simulations on pre-patient collimating optic at a wide range of energies (month 19-23)

2.1 Measure transmission as a function of x-ray energy.

2.2 Measure transmission uniformity.
2.3 Measure dependence of transmission on x-ray entrance angle.
2.4 Perform geometric simulation on transmission spectra.
Task 3: Perform experiments on collimating optic at mammographic energies. (month 24-26)
3.1 Measure exit angle divergence.
3.2 Measure contrast enhancement.
Task 4: Perform experiments and geometric simulations on post-patient anti scatter optic. (month 27-30)
4.1 Measure central part and whole optics as a function of photon energy
4.2 Measure transmission uniformity
4.3 Measure dependence of transmission on x-ray entrance angle
4.4 Perform geometric simulation on transmission spectra
Task 5: Perform experiments on post- patient anti scatter optic at mammographic energies (month 31-33)
5.1 Measure transmission energy as a function of photon energy
5.2 Measure transmission uniformity
5.3 Measure transmission entrance angle dependence
5.4 Measure scatter fraction
5.5 Measure contrast enhancement
5.6 Measure uniformity of magnification factor
Task 6. Design assessment (month 34-36)

In the first year of this project, we developed and tested a more physical model and compared the simulation results for a variety of straight capillaries to measured data in the energy range from 10 to 80 keV. Using this analysis, the number of required parameters in this energy range, including 20 keV for mammography, is reduced from four to two, bending curvature and waviness. It was not found to be necessary to include roughness effects. Although it took more than a year to develop this unexpected new model and perform its implementation for single fibers and lenses, it was worthwhile because we now have a more physical simulation model which increases the time efficiency for future modeling.

Sections 2C-2E are the comparison of the new model with the previous model and the comparison of their simulation results with the experimental data for borosilicate glass optics. During the second year the principal investigation was changed from Hui Wang to Cari. Section 2F contains measurement of a post patient scatter rejection borosilicate glass optic. Section 2G presents data and simulations applied during the second year to lead glass optics. Section 2 H present measurements and simulations of a long focal length collimating optic applied during the third year.

2.C Improvements in generating x-ray photons

As shown in Figure 3, to produce a random point P in a circle, we can randomly generate either (r, θ) or (x, y). Previous simulations[11] used uniformly generated θ in the range $(0, 2\pi)$ and r in the range (0, R), where R is the radius of the x-ray source, capillary channel or fiber input area. This work uniformly generated x and y coordinates, with the limitation $x^2 + y^2 < R^2$, which is closer to an isotropic distribution.

2.D Improvements in waviness correction model

Waviness of a capillary surface is oscillations with wavelengths shorter than the capillary length and longer than the wavelength of the roughness. The waviness effect is modeled as a random tilt of the glass wall, which results in a random change in the reflection angle on each bounce. If the random tilt angle is ϕ and the incident angle is θ, then the reflection angle with respect to the nominal surface will be $\theta+2\phi$, as shown in Figure 4. Previous simulations used a uniform distribution model; this work uses a tilt-corrected normal distribution to generate ϕ.

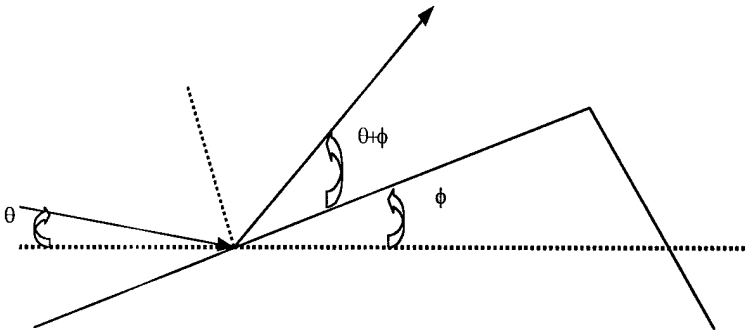

Figure 4. Scheme of an x-ray beam interactions with a randomly tilted surface.

2.D.1 Uniform distribution model

Previous simulations, referred here as Model M1, assumed a uniform distribution of 2ϕ from $-\Delta\theta_{max}$ to $\Delta\theta_{max}$ if $\theta \geq \Delta\theta_{max}$, or from $-\theta$ to $\Delta\theta_{max}$ if $\theta \leq \Delta\theta_{max}$. The maximum random tilt angle $\Delta\theta_{max}$ is the adjustable parameter which describes the amount of waviness of the capillary.

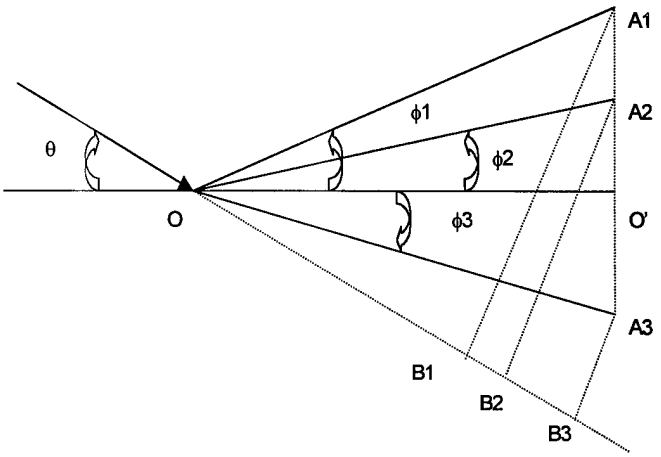

Figure 5. Three surfaces, OA_1, OA_2 and OA_3, with different tilt angles, ϕ_1, ϕ_2 and ϕ_3, respectively, from the nominal surface OO'. Here, $-\theta \leq \phi_3 \leq 0$, $OA_1*\cos\phi_1 = OA_2*\cos\phi_2 = OA_3*\cos\phi_3 = OO'$.

2.D.2 Tilt-corrected normal distribution model

2.D.2.1 Normal distribution

For this work, named as Model M2, it is assumed that these tilt angles, ϕ, are normally distributed in the range $(-\pi/2, \pi/2)$. with the mean value equal to zero. For high quality optics, the standard deviation of this normal distribution, σ, is much smaller than the critical angle, θ_c. The probability distribution of tilt angles, ϕ, is

$$G(\phi) = \frac{1}{\sigma\sqrt{2\pi}} e^{-\frac{\phi^2}{2\sigma^2}}. \quad (3)$$

2.D.2.2 X-ray impact tilt correction

In this work, Model M2, consideration was taken of the fact that the surface tilt angle will affect the probability of x-ray impact on that surface. Taken to extremes, a surface region perpendicular to the beam is much more likely to intercept the beam than a surface region parallel to the beam. Figure 5 displays three surfaces, OA_1, OA_2 and OA_3, with different tilt angles, ϕ_1, ϕ_2 and ϕ_3, respectively, from the nominal surface OO'. The projections onto the nominal surface for the three surfaces are equal, $OA_1*\cos\phi_1 = OA_2*\cos\phi_2 = OA_3*\cos\phi_3 = OO'$. The probability of incidence of a parallel x-ray beam with

incident angle θ (with respect to the nominal surface OO') hitting these tilted surfaces is given by their corresponding perpendicular length A_jB_j (for j = 1, 2 or 3)

$$P_j \propto A_jB_j = OA_j \cdot \sin(\theta+\phi_j) = \frac{OO}{\cos\phi_j} \cdot \sin(\theta+\phi_j), \quad (4)$$

We call this the tilt-corrected probability distribution. The complete description of this distribution is

$$H(\phi) = \begin{cases} \frac{F\sin(\theta+\phi)}{\cos(\phi)}, & -\theta < \phi < \frac{\pi}{2} \\ 0, & -\frac{\pi}{2} < \phi \le -\theta \end{cases}, \quad (5)$$

where θ is the incident angle, ϕ is the tilt angle and F is a normalization constant.

2.D.2.3 Tilt-corrected normal distribution

Combining the normal distribution G(ϕ) with the tilt correction H(ϕ) gives ϕ for a certain incident angle θ as follows:

$$J(\phi) = \begin{cases} Ke^{\frac{-\phi^2}{2\sigma^2}} \cdot \frac{\sin(\theta+\phi)}{\cos\phi}, & -\theta < \phi < \frac{\pi}{2} \\ 0, & \frac{-\pi}{2} \le \phi \le -\theta \end{cases}, \quad (6)$$

where θ is the incident angle, ϕ is the tilt angle and K is a normalization constant.

Noting that

$$\frac{\sin(\theta+\phi)}{\cos\phi} = \sin\theta + \cos\theta \cdot \tan\phi \quad (7)$$

and that both the incident angle, θ, and the tilt angle, ϕ, are very much less than 40 mrad, we use the approximation

$$P(\phi) = \begin{cases} Ce^{\frac{-\phi^2}{2\sigma^2}} * (\theta+\phi), & -\theta < \phi < \frac{\pi}{2} \\ 0, & -\frac{\pi}{2} \le \phi \le -\theta \end{cases}, \quad (8)$$

where the normalization constant , C, is

$$C \approx \frac{1}{\sqrt{2\pi}\theta\sigma + 2\sigma^2}, \quad (9)$$

to speed the calculation. P(ϕ) is called the tilt-corrected normal distribution. In model M2, σ is the variable that describes the amount of waviness. Two examples of J(ϕ) and P(ϕ) are shown in Figure 6 and Figure 7.

Fiber Description						Model M1				Model M2	
Fiber #	Type	Outer Diameter mm	Channel Size μm	Open Area	Length mm	z nm	s μm	R m	$\Delta\theta_{max}$ mrad	R m	σ mrad
A	1	0.5	12	65%	105	0.7	6	105	0.4	60	0.225
C	3	0.75	22	50%	136	0.5	6	125	0.35	225	0.2
D	4	4	12	55%	130	0.8	6	110	0.285	139	0.125
E	5	0.3	4-5	55%	105	0.7	6	28	0.2	31	0.09
F	4	4	12	55%	130	0.8	6	90	0.45	90	0.18

Table 1 Parameters for best-fit simulations. R is the bending radius. For M1, $\Delta\theta_{max}$ is the amount of waviness, z is the roughness height and s is the roughness correlation length. For M2, σ is the standard deviation of the waviness.

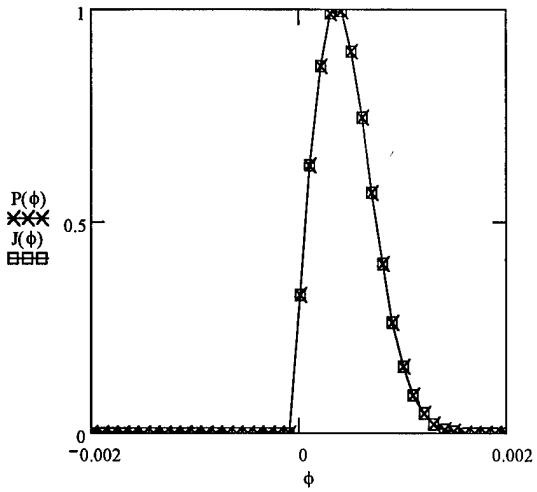

Figure 6. The probability distribution, J(ϕ), and its approximation, P(ϕ), versus tilt angle ϕ when incident angle θ = 0.0001 rad, standard deviation σ = 0.0004 rad. ϕ is in rad.

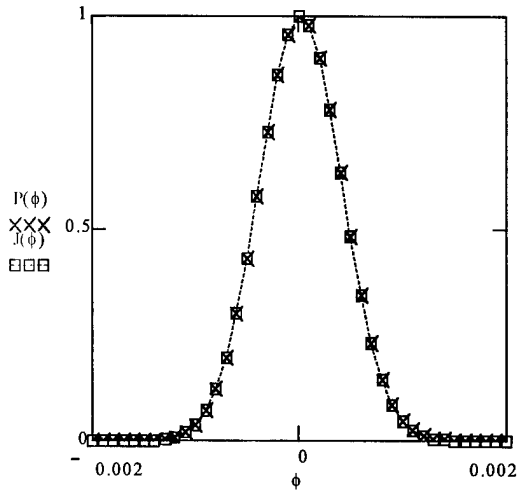

Figure 7. J(ϕ) and P(ϕ) versus tilt angle ϕ when incident angle θ = 0.009 rad, standard deviation σ = 0.0004 rad. ϕ is in rad.

2.E Results

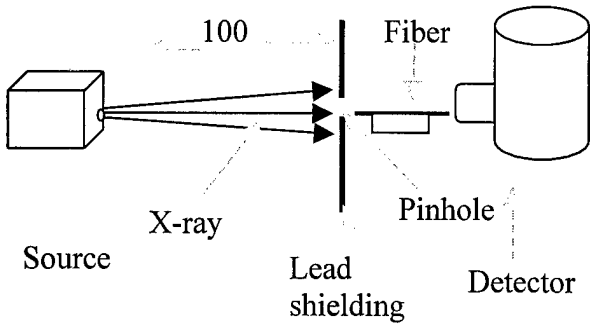

Figure 8. Experimental setup for single fiber measurement

Transmission of a number of different fibers measured previously[11] in the energy region 10-80 keV are shown in figures 9-19. The descriptions of these polycapillary fibers and their simulation parameters are shown in Table 1. The experimental setup for straight fibers measurement is shown in figure 8. A microfocus source with a tungsten target and source spot size of 50 μm was used in the experiment. The source was mounted on two stages, which could be moved in two direction transverse to the beam, and also enclosed in a thick lead box to reduce scattered x-rays. The distance between the source and the fiber was about 100 cm to ensure incident angles less than critical angle up to energy 80 keV. A 200 μm pinhole was attached to thick lead shielding. The size of the pinhole is smaller than the diameter of the fiber which is about 0.5 mm to prevent scattering and leakage, to reduce the detector dead time and to keep the distance between the source and the fiber as small as possible. The fiber was put on a finely machined groove in an aluminium plate mounted on two stages, which could be moved in two direction transverse to the beam.

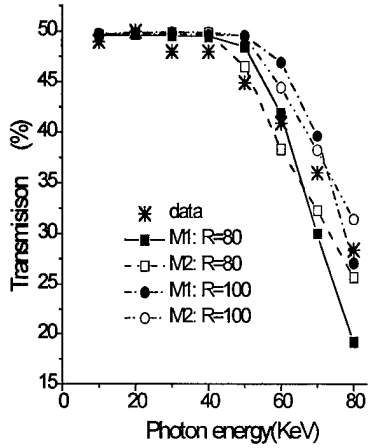

Figure 9 Transmission spectra for fiber C simulated with different bending curvature alone using models M1 and M2, compared with experimental data. This figure shows that the simulations with bending alone can not fit the data, and indicates that bending is not the only factor to cause the transmission drop.

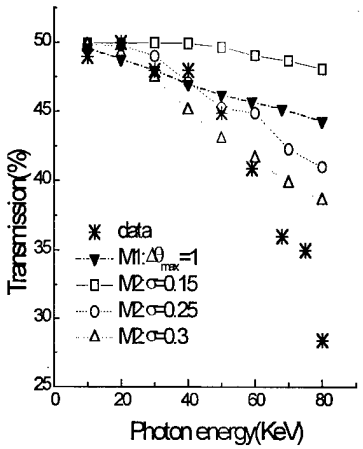

Figure 10 Simulations of transmission spectra for fiber C with only waviness compared with the experimental data. This figure shows the effects of waviness. It also shows simulations using waviness alone do not fit the data. The simulations do not include the roughness or bending correction.

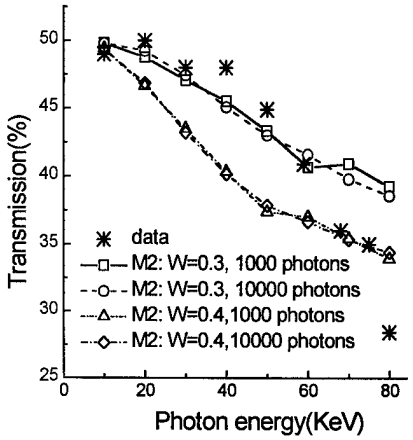

Figure 11 Simulations of transmission spectra with waviness correction using different numbers of photons, compared with the experimental data of fiber C. The figure shows that the simulation curves using 10000 photons are much smoother than those using 1000 photons because of the reduction in statistical fluctuation.

The experimental data and simulation results from the two simulations for a type 3 polycapillary, Fiber C, are compared first to demonstrate the fitting processes, to interpret the waviness and bending effects, and to understand the final results.

2.E.1 Bending effects

A slight bending can dramatically reduce the transmission of high-energy photons because of the small critical angle at high energies. Figure 9 shows a comparison between experimental data and simulations with different bend radii. The difference in the bending effect between M1 and M2 is due to the different algorithms used in generating x-ray photons as discussed in section 0. M1 assumes more photons hit the center of the fiber as well as the center of each channel. M2 generates photons uniformly across the channel, fiber and source.

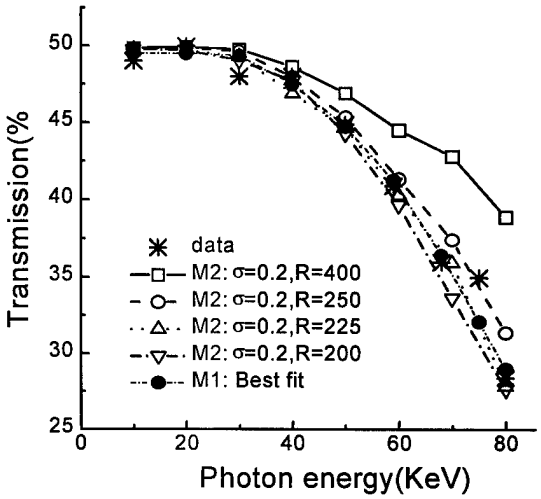

Figure 12 Simulated transmission spectra using model M2 with fixed waviness (σ=0.2 mrad) and different bending, compared with the experimental data. The simulation curves shown are just a few representative cases in the bisection process. For M2, the best-fit parameters are σ = 0.2 mrad and R = 225 m; for M1, they are z = 0.5 nm, s = 6 μm, $\Delta\theta_{max}$ = 0.35 mrad and R = 125 m.

For both models, a bend of R = 80 m reduces the transmission too much at high energies. Since any waviness or roughness correction, like the bending correction, will reduce the transmission, R must be larger than 80 meters. We set R_{min} = 80 m, which is useful in determining the best-fit parameters for the model

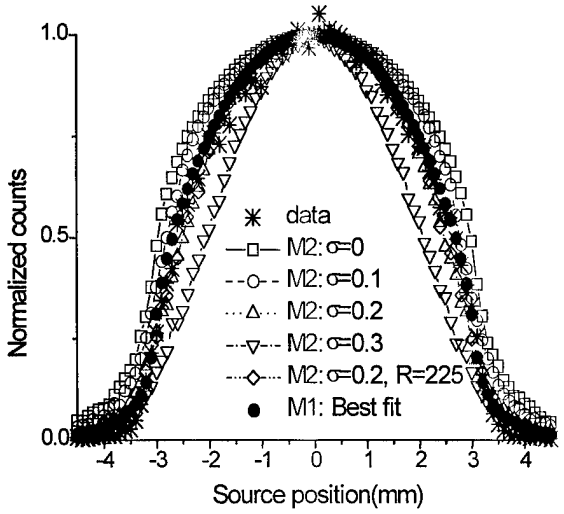

Figure 13. Simulations of source scan curve using model M2 with different waviness (σ) compared with the experimental data. The larger the waviness, the narrower the simulated scan curve. The simulation curves with the best fitting parameters of M1 and M2 obtained in Figure 12 are also shown in this figure for reference.

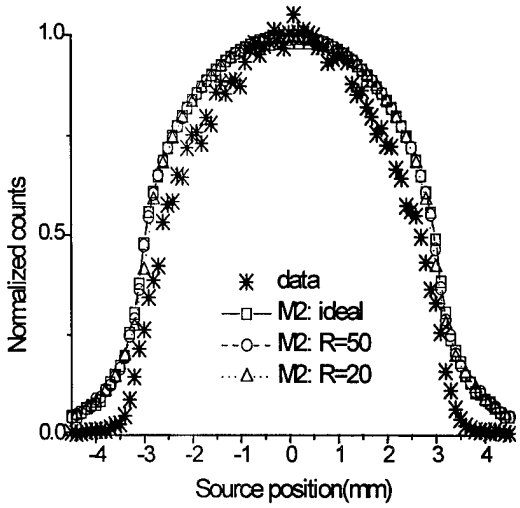

Figure 14 Simulations of source scan curves using model M2 with no waviness and different bending compared with the experimental data at 10 keV. The simulated scan curve does not become narrower even when the bending radius R = 20 m. The word "ideal" refers to a simulation with R=∞ and no waviness.

M2. Clearly, bending alone cannot explain the experimental data, especially at low energies.

2.E.2 Waviness effects

To explain the data at energies from 20 to 60 keV, another correction is needed. Roughness does not have a major effect in this energy range[11]. Waviness is expected to be the major factor in this energy range.

Figure 10 shows that the transmission becomes lower for all the energies and the high-energy transmission drops faster with increasing σ gets larger. It also shows that waviness alone, like bending alone, can not explain the experimental data. In the simulation, σ = 0.3 mrad and 0.4 mrad are definitely over-correcting at low energies, so we can set 0.3 mrad as the maximum of σ (σ_{max}) for Fiber C. The waviness parameter Δθ for model M1 is larger than the parameter σ for model 2 because the tilt correction in model M2 makes it more probable that the x-ray will intersect the high angle surfaces.

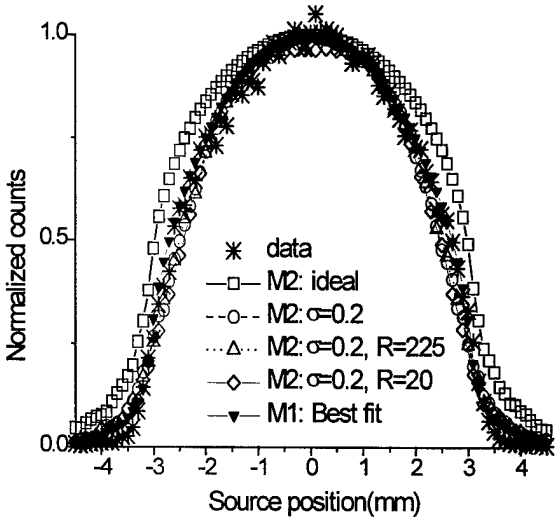

Figure 15 Simulations of source scan curves using model M2 with fixed waviness (σ = 0.2 mrad) and different bending compared with the experimental data. The simulated scan curve does not apparently change even when the bending radius R = 20 m. With and without the bending, simulations using σ =0.2 mrad fit the experimental data quite well.

The fluctuation of the simulation curve in Figure 10 when σ=0.25 mrad is mainly due to the relatively small number of photons, 1000, used in the simulation. Figure 11 shows the difference when the number of photons changes from 1000 to 10000.

Using a bisection algorithm with R_{min} and σ_{max}, R and σ were applied together and compared to the data to get the best fit parameters, as shown in Figure 12. The best fit parameters for fiber C using model M2 are R = 225 m and σ = 0.2 mrad.

2.E.3 Verification using the source scan curves

Figure 13 shows the source scan curve, that is transmission as a function of lateral source displacement, and simulation results, for increasing waviness for Fiber C at 10 keV. The simulated source scan slowly becomes narrower when σ gets larger, however that change is too small to be used to determine σ. *Figure 14* displays simulations for Fiber C at 10 keV with different R and no waviness. *Figure 15* shows the effect of different R with a fixed σ. From these two figures, it is apparent that changing R from 20 meters to infinity does not have any visible effect on the fitting curve. Therefore, we can not use the simulations of the source scan curves to determine either σ or R, but they can be used to verify σ.

For Fiber C, as shown for 10 keV in Figure 13, at higher energies in Figure 16, and as a function of energy in Figure 12, the simulation curve of σ=0.2 mrad fits the experiment data very well with one fewer fitting parameter than the best fit of M1.

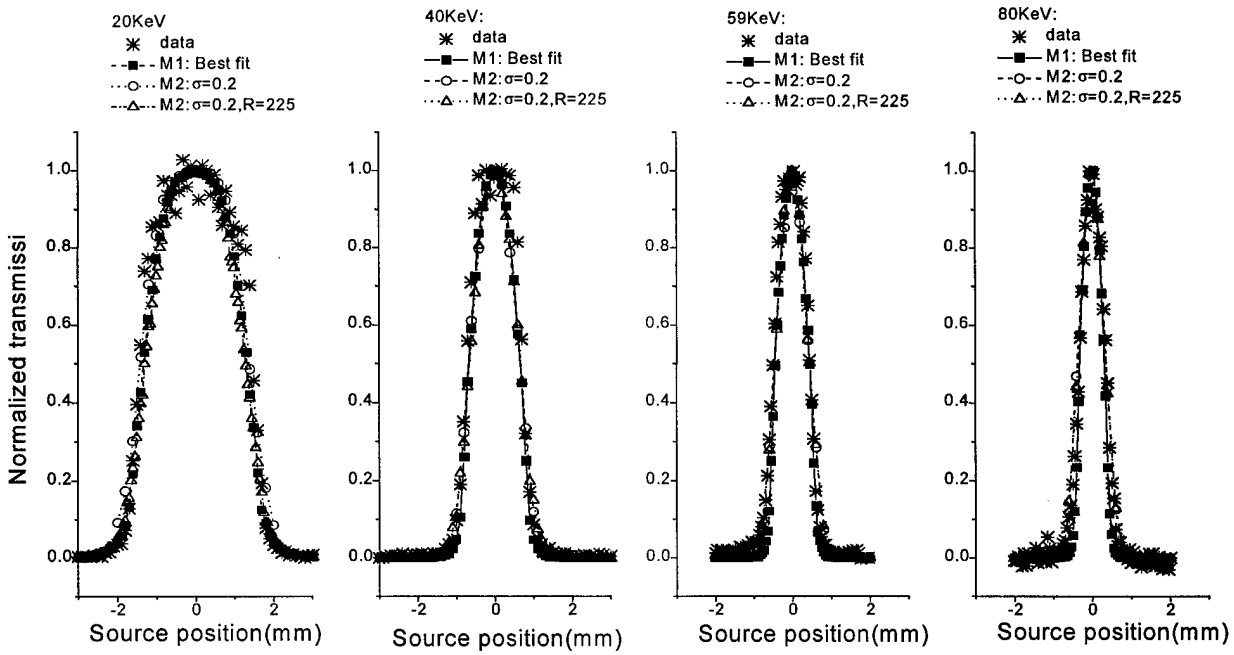

Figure 16 Simulated source scan curves using M1 and M2 compared with experimental data at four different photon energies. They all fit the data quite well. For M2, this figure also verifies that the bending has no visible effect on the source scan. The best-fit parameters for M1 are R = 125 m, $\Delta\theta_{max}$ = 0.35 mrad, s = 6 μm and z = 0.5 nm.

2.E.4 Best-fits of all the fibers and analysis of the results

Using the algorithm described above, the best-fit parameters of M2 for Fiber A, D and E were obtained. The best-fit parameters for both M1 and M2 are shown in Table 1. The best-fit curves of M1 and M2 along with the experimental data are shown in Figures 17-19. The fibers are described in *Table 1.*

In Figure 18, the transmission for fiber A shows a rapid drop for energies above 30 keV. Although fiber D has lower fractional open area than fiber A, its transmission exceeds that of fiber A at energies above 30 keV. This is because fiber A is thin (0.5 mm in outer diameter) and flexible, therefore difficult to keep straight in the measurement apparatus. Model M2, which can vary only bending and waviness, requires a much sharper bend for fiber A than for fi-

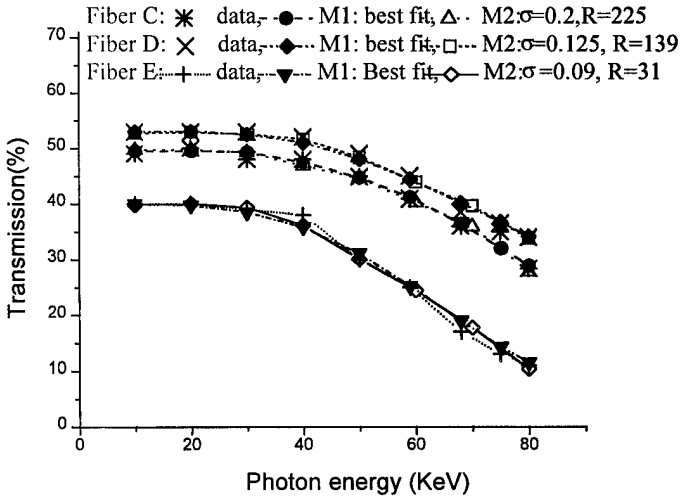

Figure 17. Simulations of transmission spectra of fiber C, fiber D and fiber E with their best-fit parameters compared with the experimental data. All parameters related to this figure are listed in Table 1.

ber D. This bending is more significant at high energies, where the critical angles are smaller.

Transmission curves for fiber C and D are similar in shape and are nearly flat up to 60 keV, as shown in figure 16. However, the smaller channel size for fiber D results in the simulation being less sensitive to bending. Therefore a larger bending curvature (smaller radius) is required for fiber D. The waviness correction for fiber D must therefore be smaller to keep the transmission about the same as for fiber C.

Fiber E is the thinnest fiber. Table 1 shows that it has the largest bending correction because of its flexibility. Its transmission curve is flat up to 40 keV. This is due to its very small channel size, as discussed in the comparison of fiber C and fiber D. However, if the channel size is too small, as in fiber E, it also results in more reflections being needed for a photon to traverse the fiber and may have introduced other defects such as blocked channels. This is why the transmission is only 40% for the energies below 40 keV although the open area is around 55%.

The high transmission and the simulation results show that the quality of the capillary fibers is quite good. The bending radius is above 130 meters for type 3 and type 4 capillaries. It is hopeful that we can further improve the high-energy transmission performance of polycapillary fibers by decreasing to an optimum channel size, and making them more rigid.

Because Model M2 is physically plausible, gives reasonable results, and matches the experimental data very well, as shown in figures 17 and 18, we can use it to simulate other poly-

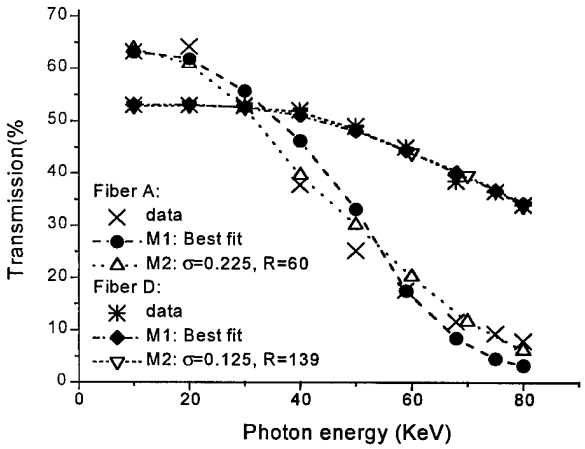

Figure 18. Simulations of transmission spectra of fiber A and fiber D with their best-fit parameters compared with the experimental data. All parameters related to this figure are listed in Table 1.

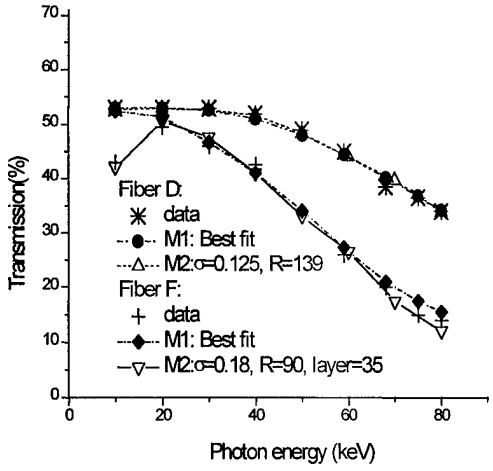

Figure19 Simulations of transmission spectra of fiber D (unexposed) and fiber F (exposed) with their best-fit parameters compared with the experimental data. Layer = 35 means that there is a 35 micron glass layer added. All parameters related to this figure are listed in Table 1 except the glass layer.

capillary optics. Compared to M1, which uses four parameters, M2 uses only two parameters, which makes simulating the experimental results more straightforward, easier and timesaving. In addition, roughness does not have much effect in the energy range 10-80 keV, so M2 gives us more confidence with fewer parameters.

2.E.5 An analysis of a radiation-damaged fiber

The measured transmission spectra and source scans provide sensitive tools for analyzing capillary quality. This method was used to analyze the effect of radiation damage on fiber F that has the same type and same length as fiber D. Radiation damage has been

observed after a very large dose of x-ray exposure.[12] It was found that prolonged exposure to synchrotron white beam radiation could cause a measurable bend for a thin fiber. This bending can be reduced by annealing and by holding the fiber rigid during exposure. Fiber F had 1.8 MJ/cm^2 exposure before the current measurements. There is no visually observable bending or other visible damage.

The transmission spectrum and its simulation for fiber F are compared with an unexposed capillary of the same type, fiber D, in Figure 17. The measured data shows a significant transmission drop above 30 keV and below 10 keV. The simulation indicates that the exposed capillary has more bending and waviness. The bending radius was changed from 139 m to 90 m and the waviness σ changed from 0.125 mrad to 0.18 mrad. Although these profile changes have a significant effect the transmission, they are still very small and not visible. The transmission drop below 20 keV can be explained by adding 35 μm x-ray-absorbing glass layer as shown in Figure 19.[13]

2.F Measurement of a prototype post-patient monolithic optic

Polycapillary optics can be used for post patient scatter rejection. Off-axis rays are not transmitted down the optic, as shown in figure 15. Monolithic optics are shaped from a single large fiber. The basicgeomtric of this post-patient monolithic optic as a cone with length of the optic =129 mm, output diameter= 8.25 mm, input diameter=6.1 mm, channel size = 25μm and focal distance = 500 mm.

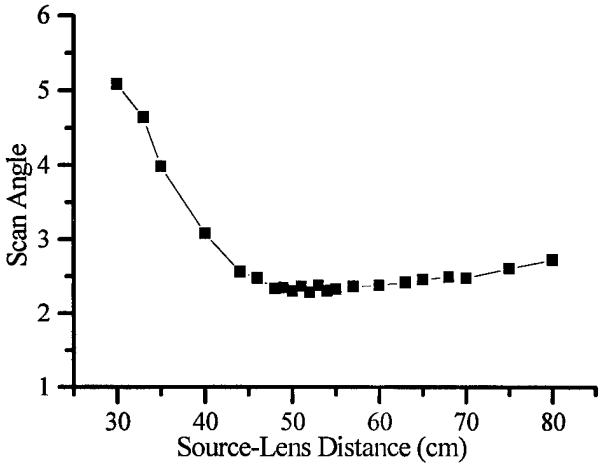

Figure 20. Measured acceptance angle as function of source-optic distance for the monolithics optic at 20 keV

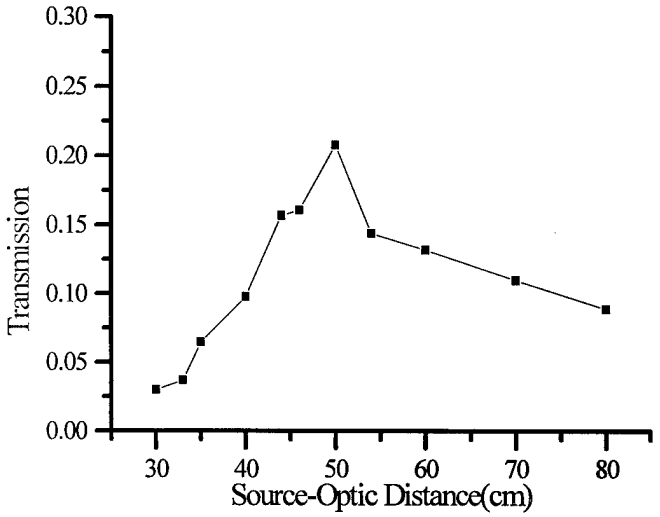

Figure 21. Measured transmission vs source-optic distance at 20 keV.

The x-ray generator used in the experiment is the same as for the previous section. Variation of acceptance angle of the optics as a function of source optic distance was used primarily to determine both focal distance of prototype monolithic optic and the input depth field. The acceptance angle is the full width half maximum of the source scan divided by the source to optic distance. The full width half maximum will describe the maximum diameter of a source over which optic will collect efficiently and the intensity transmitted through the optic follows a gaussian curvature as shown in figure 22. The acceptance angle is a minimum at the focal distance, where the transmission is maximized. Focal distance

of this optic was determined by moving the source in x and y direction to maximize the transmission at certain position of the optic. The highest transmission as the input focus distance, and the full width at ¾ of the maximum is defined as the depth of field.

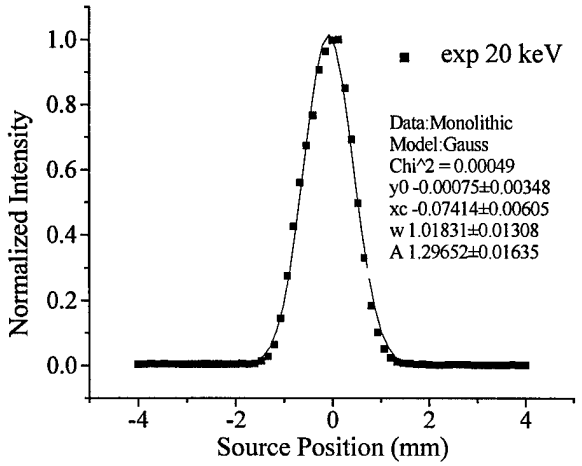

Figure 22. Measured scan source at the focal distance.

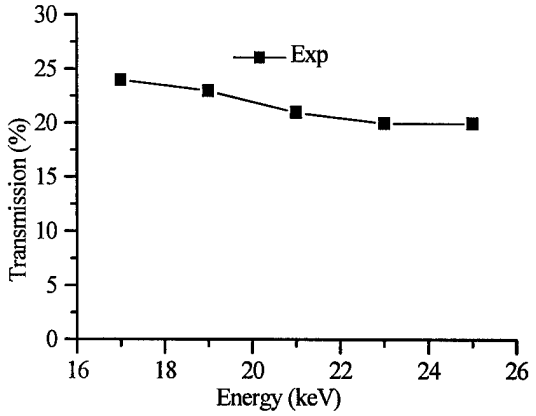

Figure 23. Transmission versus energy at the focal distance

Figure 21 shows that the focal length and the depth field of this optic are 500 mm and 92 mm, respectively. This focal length is in good agreement with the focal length determined by using the transmission as function of source to optic distance, as shown in figure 21. The high angle transmission of this optics close to zero, as can be seen in figure 22 when the source is moved off-axis. This will give good scatter rejection. Finally, the transmission efficiency of this optic was measured at the focal point, as in figure 23. However the transmission of the long optic is poor.

2.F Measurement and analysis of leaded glass fibers

Leaded glass polycapillary optics could be a candidate for scatter rejection because of lead's superior absorption. Lead glass optics could be shorter and therefore easier to manufacture with better transmission. Lead glass optics may be the fast way to be bring capillary optics to clinical use. In this section, we will analyze the experimental results of a number of leaded glass single capillaries using model M2. Transmission of a leaded glass polycapillary in the 9-80 keV energy range is shown in figure 24. The description of these capillaries and the simulation parameters are listed in table II. The characteristics of the transmission spectra of a leaded glass fiber are similar to the radiation-damaged borosilicate fiber, i.e, the transmission drops off at both lower energies and higher energies, as shown in figure 24. In addition to the waviness and bending simulation parameters, the simulation has to include a leaded glass layer of 33 μm thick and roughness 1.7 nm to fit the experimental data.

Fiber					Simulation			
Fiber type	Outer Diameter mm	Channel size μm	Open area %	Length mm	Bending R m	Waviness w mrad	Layer t μm	Roughness z nm
A	0.53	12	60	60	40	0.26	45	1.8
B30	0.51	12	60	30	30	0.15	18	1.7
B60	0.51	12	60	60	56	0.15	33	1.7
C	0.51	11	50	60	27	0.19	33	1.8
D	0.53	11	50	60	28	0.20	43	1.8
E	0.53	11	40	60	45	0.28	47	2.1

Table II. Fiber description and simulation parameters

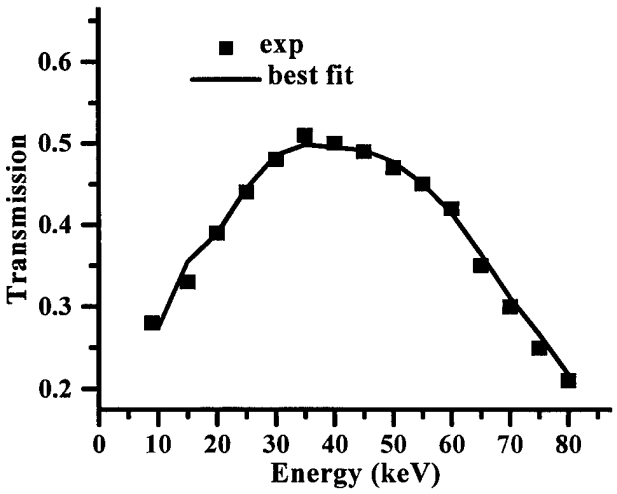

Figure 24. Simulated transmission with and without leaded glass filter for type B60 fiber are compared with the experimental data. Best fit is simulated transmission with R=56 m, w=0.15 mrad, z=1.7 nm, and t=33μm.

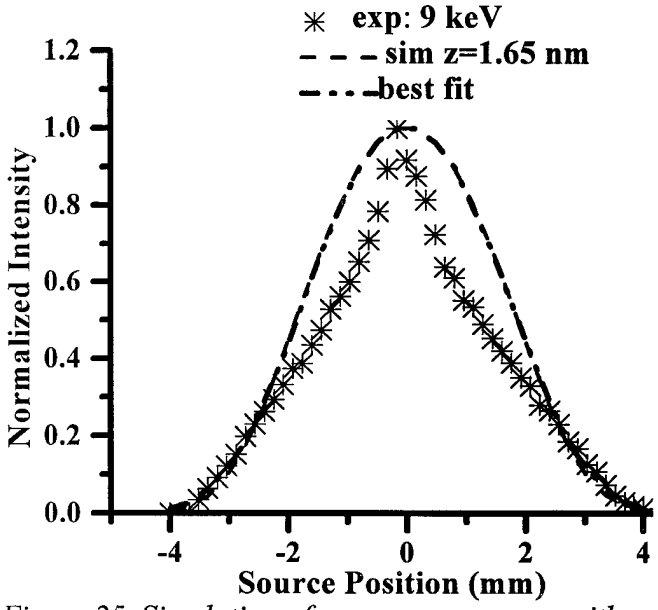

Figure 25. Simulation of source scan curves with z=1.7 nm , R=56 m, and w=0.15 mrad, and with roughness z=1.7 nm alone, compared with the experimental data. Since the actual transmission at this energy is quite low, the source scan curve might be somewhat distorted, and thus the simulation does not fit the data well.

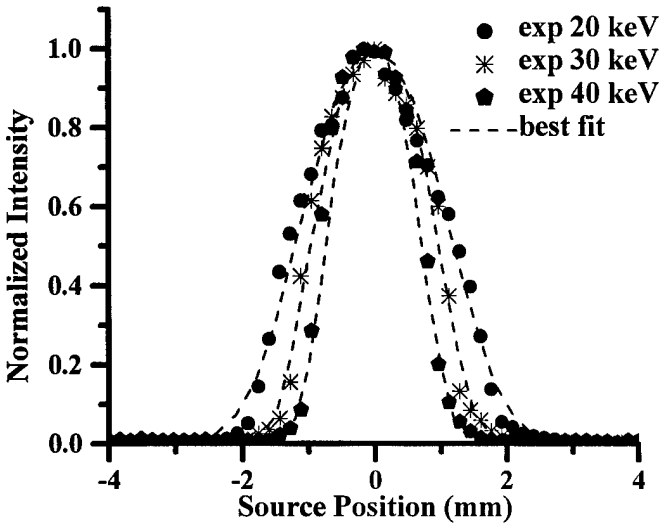

Figure 26. Simulated scan curves compared with the experimental data at three photon energies.

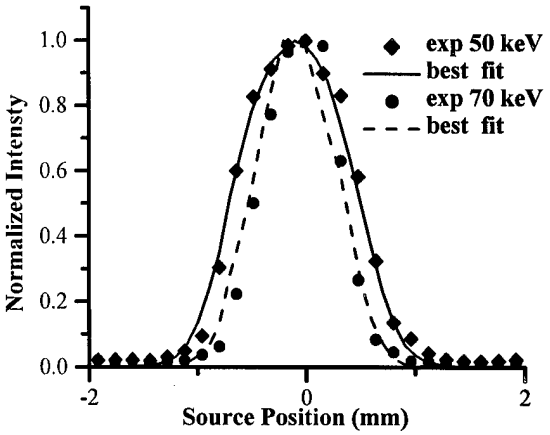

Figure 27.The simulation of scan curves with best fit parameters at 50 and 70 keV, compared with the experimental data.

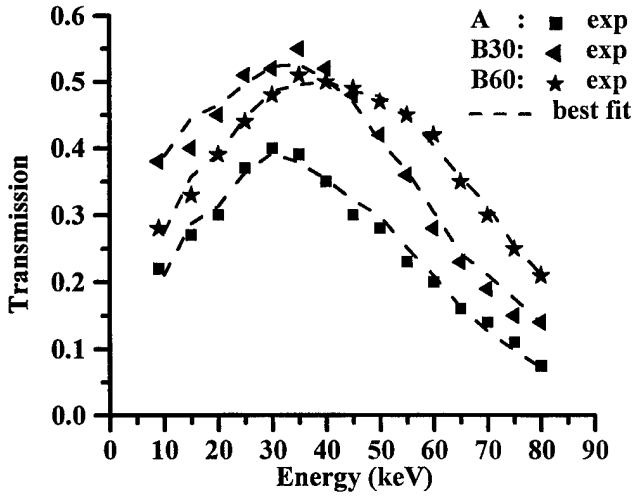

Figure 28 Simulation of transmission spectra of fiber A, fiber B60 (B with length of 60 mm) and fiber B30 (B with length of 30 mm) with their best fit parameters listed in Table II, compared with the experimental data.

The best fit simulation compared with the experimental data for source scan curveare shown in figure 25-26. At 9 keV the simulated for source scan does not fit, as shown in figure 25. This may be partly because the actual value of the transmission at 9 keV, as shown in figure 24, is quite low. But the simulation at high energies for source scan curve were fit the data fairly well.

Finally, the measured transmission spectra for a number of leaded glass fibers II are shown in figure 28.

The models fit the transmission spectra well, with the parameters listed in table II.

2.H. Measurements and Analysis of a Long Focal Length Collimating Lens

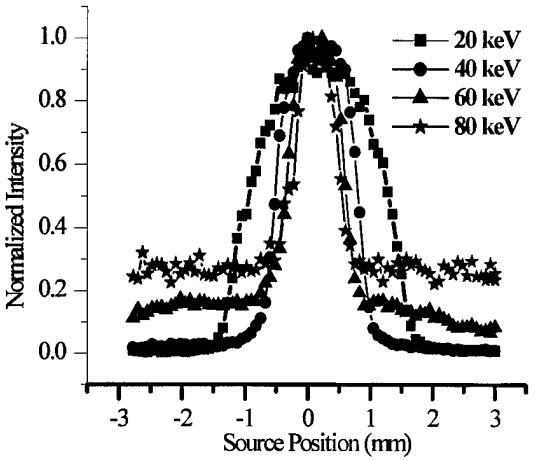

Figure 29. Measured source scan curve from 20 – 80 keV. The figure shows that there was no x-rays leakage.

Another use of polycapillary optics is beam shaping, collimation, image demagnification were measure using a multifiber borosilicate optic. Each single fiber is about 0.51 mm in diameter, and contains hundreds or thousands capillary tubes, 10 μm in diameter. The multifiber polycapillary optic was constructed by stringing 3039 flexible single fibers through metal holding grids. The fibers at one end of the lens are parallel, and at other end are pointed toward a common focal point, 2 m away. This means that this lens can be used to collimate or focus x rays. In collimating mode, the lens is used as a collimator to collect x-rays from a point source at the focus and produce a nearly parallel beam. In focusing mode, the lens is used as a collector for parallel a beam input and produce a focused beam. The focused beam can be used to demagnify an image. This is of potential benefit for direct imaging with small area digital x-ray detector.

The focal length, transmission efficiency, uniformity, and exit divergence were measured in collimating mode. Scatter rejection, contrast enhancement, and demagnification were demonstrated in focusing mode.

2.H.1 Single Fiber Measurements and Analysis

2.H.1.a Straight Fiber

To ensure that source, pinhole, fiber and detector were aligned well, the transmission as a function of source location was measured, as shown in figure 29 for a fiber with length of 140 mm. The figure shows that there was not any x-ray leakage detected. Then the transmission of the fiber type used to construct a collimating lens were measured in the 10-80 keV energy range. Several fibers of different lengths were measured, three fibers from which are presented in figure 30. The fractional open area of the fiber is 70 ± 3 %.

2.H.1.a.1 Simulation Analysis

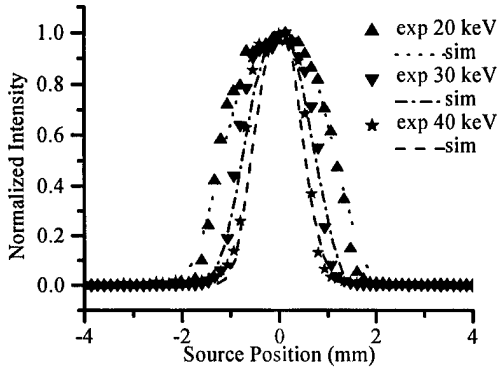

Figure 30. Source scan with length of fibes is 140 mm. The lines are simulated data with waviness, w=0.12 mrad, roughness, z=0.65 nm, and bending, R=210 m

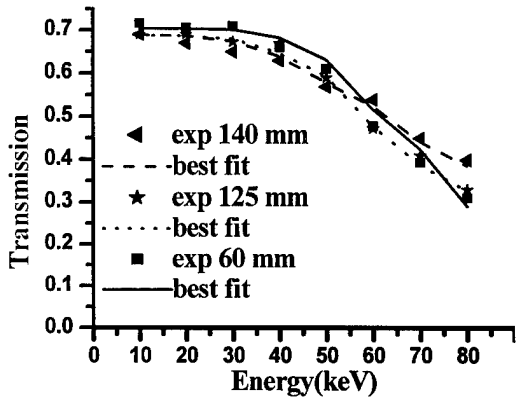

Figure 31. Transmission versus energy for single fibers with three different lengths. The lines are simulated data with waviness w= 0.12 mrad, and roughness z= 0.65 nm, but with different bending curvature, R_{140}=210 m, R_{125}=105 m, R_{60}=48 m.

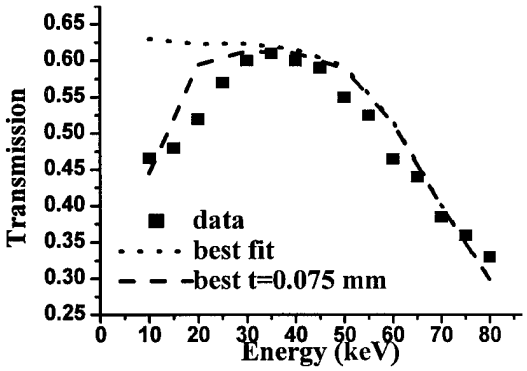

Figure 32. Simulated transmission compared with the experimental data for a defected a fiber. Best fit is simulation with waviness w=0.12 mrad, roughness z=0.65 nm bending radius R=54 m, and glass layer thickness, t=75 μm.

The experimental data then was analyzed using the geometrical optic simulation model M2 to understand the performance of the fibers. The best fit simulation parameters were determined in the manner of section 2 E. Using waviness from the source scan curve at 30 keV, roughness from source scan curve at 10 keV and adding a bending radius of 210 m, a fit was achieved across the whole spectrum. The simulated source scan curves with these three best fit simulation parameters for a 140 mm long fiber compared with the experimental data is shown in figure 30. Then the fitting processes were applied to two fibers with length of 125 mm and 60 mm. The simulated transmission spectra for these three fibers compared with experimental data are also shown in figure 31. Each simulation fits the experimental data well. Since the fibers are thin, a shorter fiber bends more and therefore transmits somewhat more poorly at high energies. All three lengths of fibers shown in figure 31 have good transmission up to energy 50 keV.

2.H.1.a.2 Defected Fiber

One of the measured fibers contained defects which caused the transmission to drop at low energies. The fiber was cut into two parts and their transmission was measured. One 60 mm long part also has low transmission at low energies, as shown in figure 30. It was suspected that the channels were blocked by glass layer of thickness t. The simulation, with waviness of 0.12 mrad and roughness 0.65 nm obtained

in single fiber simulation previously, and adding the bending with radius of 54 m, fits the transmission spectrum data at only mid and high energies. Including a glass layer of thickness of 75 μm into the simulation, the simulated transmission fits the data quite well, as shown in figure 32. Therefore, the drop in transmission at low energies could be caused by glass inclusions in the channels.[2]

2.H.1.b Bent Fiber

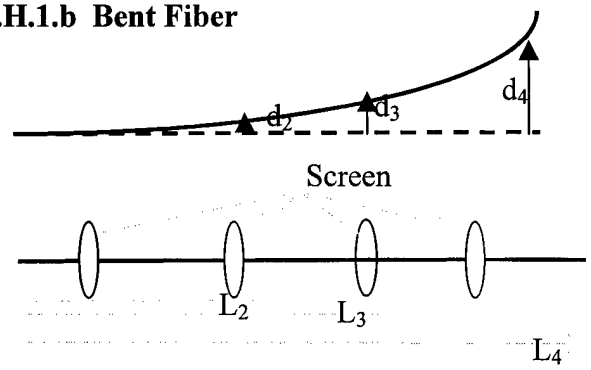

Figure 33. Sketch of fiber displacements for uniform bending measurements.

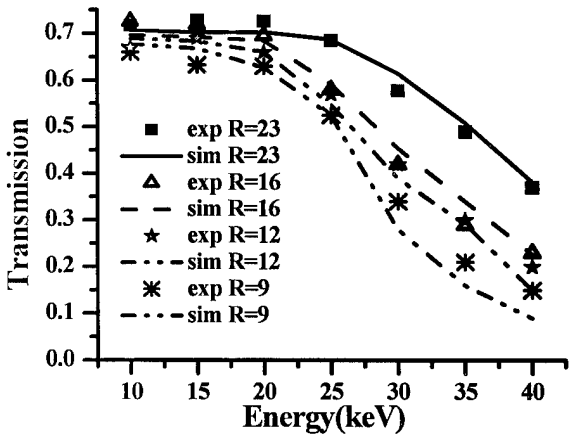

Figure 34. The simulated transmission compared with the experimental data for deliberately bent fiber. The lines are simulated data with waviness w=0.12 mrad, and roughness z= 0.65 nm, but with different bending radius R.

In the straight fiber measurements, as shown in figure 8, the fiber was designed to be straight in the experimental setup. However, the fiber experienced unintentional bending because it was so thin. The bending radius was determined from the simulated transmission, fit to the experimental data. In the bending experiment, the fiber was inserted into four metal screens, as shown in figure 33. Initially, the fiber transmission was maximized and the transmission was measured and analyzed using the geometric simulation as for the straight fiber. The bending radius found from the simulation was called initial radius Ro and thus produced an initial fiber displacement from an ideal straight path. Then the fiber was bent intentionally by moving the actuator supporting the screen as in figure 33. The nearest screen to the input end of the fiber was fixed. Each screen displacement d_{move} was calculated such that the fiber bent in a uniform circle. The relation between the bending radius, R, and the screen displacement, d_{movei}, is $R = L_i^2 / 2\, d_{movei}$, where L_i is the length of the fiber from the input end to the i^{th} screen. In the initial measurement, the fiber had been bent unintentionally with a radius R_o which resulted unintentional displacement d_{oi}, if then the fiber is displaced by d_{movei}, the total displacement of the fiber at the i^{th} screen is $d_i = (d_{oi} + d_{movei})$. A fiber with length of 140 mm was measured in the bending set up. The initial position, the fiber assumed to be straight, was found from simulation to have an unintentional bend with radius 35 m. Deliberate bends of R=9-23 m were measured. The simulation, with this intentional bending radius, and using the waviness and roughness from straight fiber simulation (w=0.12 mrad and z=0.65 nm), fits the data quite well, as shown in figure 34. The good agreement between the computer models and the single fiber data allows accurate design and prediction of optic behavior.

2.H.2Collimating Lens Measurements and Analysis

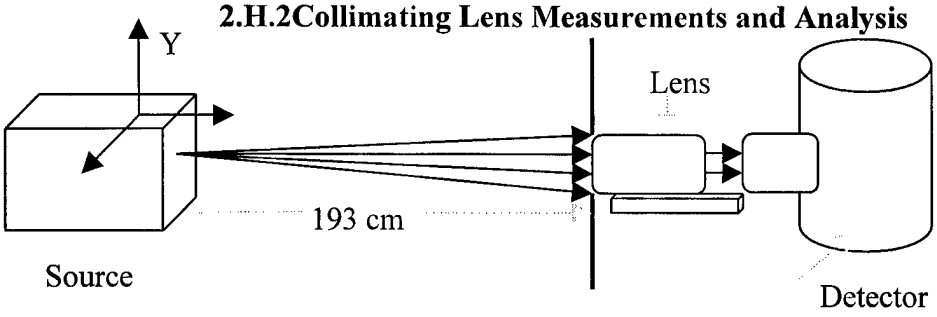

Figure 33. Experimental setup for transmission measurement of lens.

A long focal length multifiber collimating lens with a length of 140 mm, input size of 29 mm X 29 mm and output size 30 mm x 30 mm was measured. The fibers were close-packed at the input end of the lens. The fiber packing fraction at the output end of the lens was 76.5%, therefore the total open area of the lens, including the individual fiber open area of 70%, was 54%. The lens was tested in both focussing and collimating mode. The focal length, transmission efficiency, uniformity and exit divergence were measured in collimating mode. Scatter rejection, contrast enhancement, and demagnification was demonstrated in focussing mode. In this mode the detector can be smaller than the object imaged.

2.H.2.a Collimating mode

The experimental setup to measure focal length, transmission efficiency, and uniformity of the lens, is shown in figure 35. The source was 193 cm from the input of the lens, the detector was 1 cm from the output of the lens.

2.H.2.a.1 Focal length

The focal length of the lens is the location at which the transmission is maximized. Transmission at different distances and energies are shown in figures 36a and b. The measured focal length of the lens was 193±1 cm. An image of the x-ray output of the lens with this source distance is shown in figure 35.

2.H.2.a.2 Transmission

Transmission as a function of energy was measured. To explain the experimental results, a geometric simulation for single fibers was extended to simulate the lens. The bending radius of fiber at each location in the lens was calculated using a simple geometric formula. The number of fibers with each bending radius was determined. Putting together

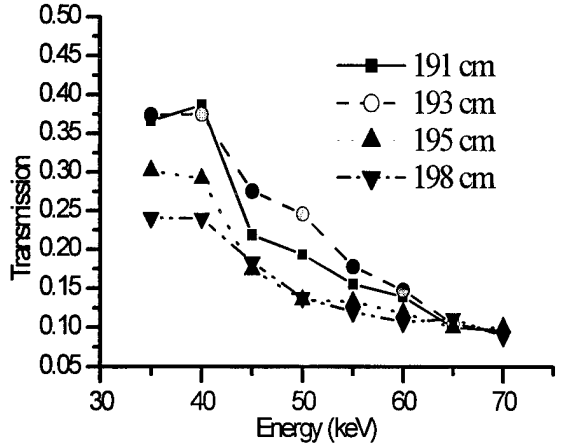

Figure 34a. Transmission vs energy with difference source-lens distances. The transmission is maximized at 192±1 cm.

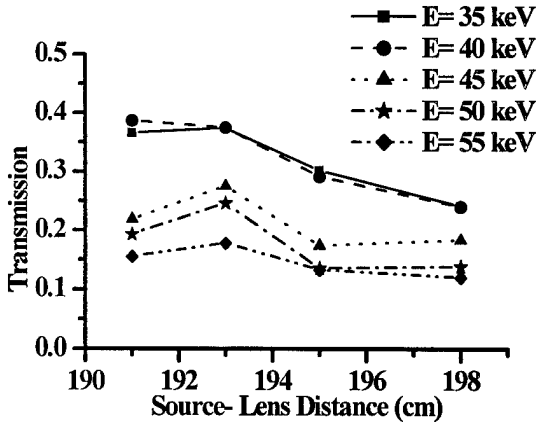

Figure 34b. Transmission versus source-lens distance at various energies. For all energies, the transmission is maximized at a 192±1 cm.

all three simulation parameters, waviness and roughness from the single fiber simulation, and bending radius calculated at each fiber location in the lens, the simulated transmission spectrum was obtained. The simulated transmission spectrum for the whole lens is the average transmission spectra of all the locations normalized with the total fractional open area of the lens. The simulated transmission spectrum compared to experimental data is shown in figure 38. The simulated transmission fits the experimental data better at higher energies than lower ones since the channels of some fibers in the lens were blocked by glass inclusions.[1,2] The lens has good transmission up to 40 keV, and therefore seems promising for low and mid range energy applications, such as mammography, astronomy and angiography.

2.H.2.a.3 Uniformity

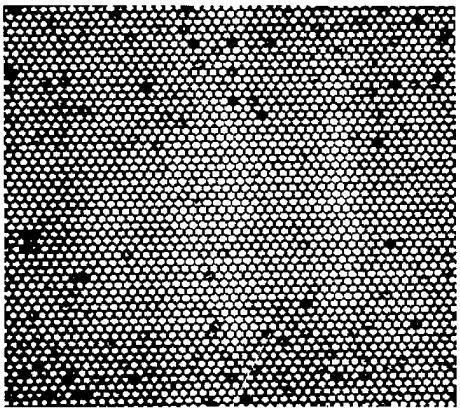

Figure 37. Photograph of the output of the lens with the source at the focal distance.

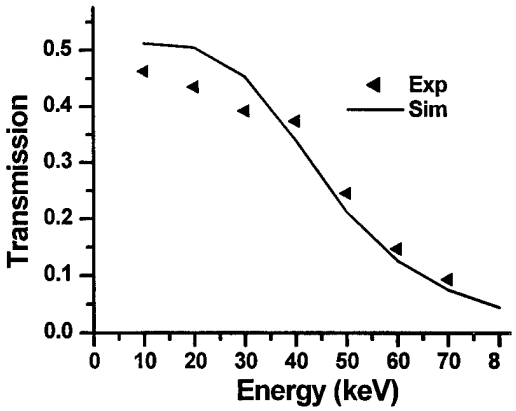

Figure 38. Simulated transmission compared to experimental data for the long focal length collimating lens.

Figures 39 and 40 are two-dimensional output scans of the lens at 20 keV and and 45 keV, respectively. These were recorded by moving a 5 mm diameter aperture in two directions perpendicular to the lens axis,

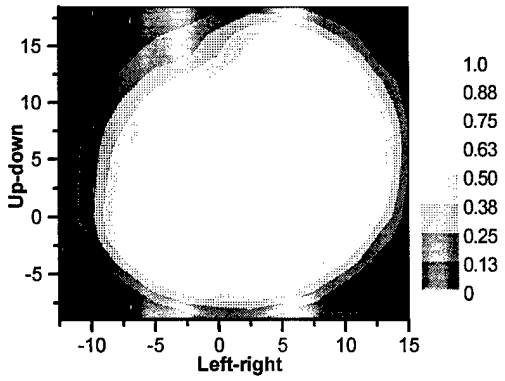

Figure 39. Output intensity from two-dimensional scan of lens output at 20 keV before some parts of the fibers changed.

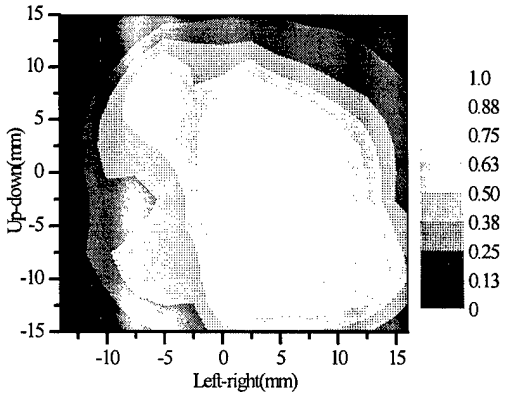

Figure 40. Output intensity from two dimensional scan of lens output at 45 keV

with source, lens, and detector fixed. The higher the energy, the lower the transmission of the outer edges of the lens. This is expected, because of smaller critical angle at higher energies.

2.H.2.a.4 Exit Divergence

Measurements of the exit divergence of the collimating lens were performed at 17.5 keV with a Mo source and NaI detector as shown in figure 41. The total divergence was measured by rocking a (100) silicon wafer in the beam, using the (400) Bragg diffraction, without any aperture at the exit of the lens. The results of the total exit divergence are shown in Figure 42. Local divergence was measured with a 9.5 mm diameter aperture at upper left (ul), upper center (uc), upper right (ur), center left (cl), center (c), center right (cr), bottom left (bl), bottom center (bc), and bottom right (br) on the exit of the lens. The results of the local divergence are shown in Table III. In general, the divergence is low, which requires that the fibers are very parallel at exit. Some areas (uc and bc) had poor alignment, and the fibers were replaced. The average local divergence is in agreement with the value of the total divergence, 1.2 mrad.

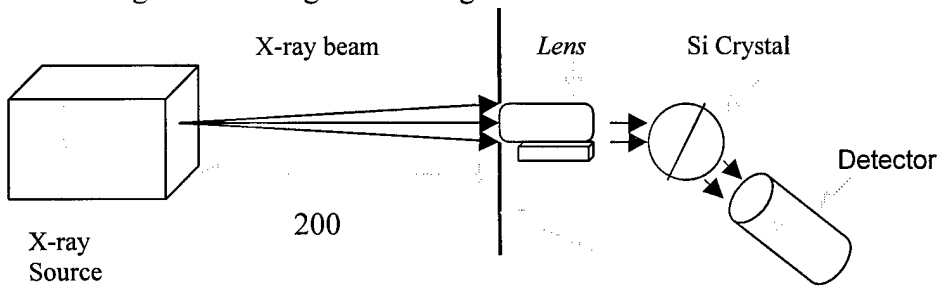

Figure 41. Experimental setup for exit divergence of lens

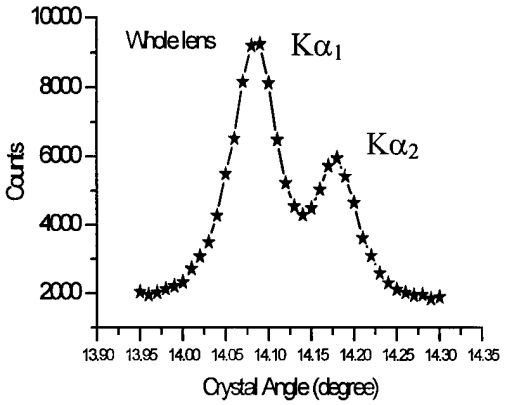

Figure 42. Total divergence rocking curve. The first peak is diffraction of the Mo $K\alpha_1$ and the second the Mo $K\alpha_2$ characteristic lines. The FWHM of the first peak was 1.2 mrad.

Local divergence		
UL=1.2	**UC=1.5**	**UR=1.0**
CL=0.9	**C=0.9**	**CR=1.1**
BL=1.2	**BC=1.5**	**BR=1.3**

Table III. Local exit divergence, in mrad, at the nine aperture locations.

2.H.2.b Focusing Mode

In focusing mode, the focusing end of the lens faced the detector, thus the lens acted as a collector to the incoming parallel beam. Testing of this lens was performed at the Stray Light Facility (SLF) at Marshall Space Flight Center (MSFC) in Huntsville, Alabama where a very parallel source beam was available, as shown in figure 43. X rays from a copper source enter a vacuum tube 100 m in the length and exit into the testing area. Measurements at the stray light facility are complicated by the low count rate of the photons because of the huge source-to-detector distance. Data was collected over a 10 keV energy window 15-25 keV, to increase the count rate.

2.H.2.b.1 Contrast and scatter rejection measurements

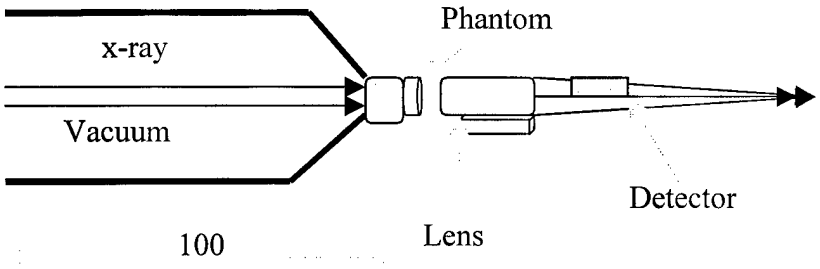

Figure 43. Experimental setup for contrast and scatter measurement.

Contrast is defined as the log of the ratio of the intensity through the area of interest to the intensity of the neighboring background.

$$C = \ln (I_p/I_{bg}) \qquad (10)$$

where I_p is the intensity through object of interest, and I_{bg} is the neighboring background intensity. Contrast is reduced by the presence of scattered x rays which emerge at all angles from the patient and form a background fog. Contrast with scatter

$$C_s= \ln\{(I_p+I_s)/(I_{bg}+I_s)\}, \qquad (11)$$

where I_s is the intensity of the scatter.
Scatter fraction is defined as

$$SF= [I_s/(I_s+I_p)] \qquad (12)$$

Scatter can be removed from the beam by either an air gap or a polycapillary optic. The introduction of an air gap causes the intensity of the isotropic scatter radiation to drop faster than the forward-directed primary beam. For conventional sources, air gaps hurt resolution because the geometric blur from the finite source increases with object to detector distance. Here, the parallel beam has very low geometric blur. Alternatively, the scatter radiation, which emerges from the phantom at high angles, can be absorbed by the glass walls of the polycapillary optic, as shown in figure 44. Only the forward-directed primary beam is carried down the channels.

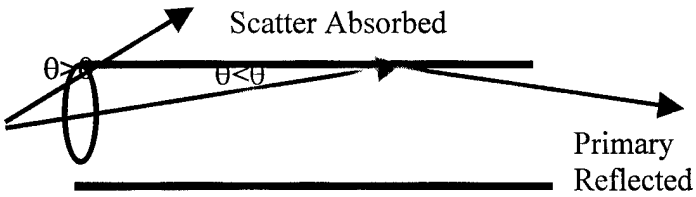

Figure 44. Mechanism photons of x rays through the glass wall

Contrast and scatter fraction measurements were performed in focusing mode as shown in figure 41 with a detector-lens distance of 20 cm. The scatter fraction was measured by placing a lead block in the beam and measuring the scattered fog intensity behind the block due to a 2.5 cm thick Lucite phantom. By scanning the detector, the scatter intensity behind the block can be measured, as shown in figures 45 and 46, with parallel air gap and lens, respectively. The polycapillary lens is even better than the parallel beam air gap at removing the scatter. To measure contrast, a 1 cm thick Lucite phantom with holes of different diameter and depth was attached on the output of the vacuum chamber. Two cases were measured. In the first, air gap case, the lens was removed and detector was placed 34 cm from the phantom. Because the air gap removes most of the scatter, the contrast is good. In the second case, the lens was put in place and detector inserted 20 cm from the lens. Distance between the phantom and the lens was 3 cm. In both case, the output was scanned using a small (3 mm x 3 mm) detector. The intensity was measured for 60 seconds at each location, and the data assembled as an image, as shown in figures 47 and 48. The contrast was determined from the measured intensity behind and near each hole and is shown in table IV. Contrast was also calculated from the theoretical attenuation in the plastic, corrected for the known scatter fractions. In each

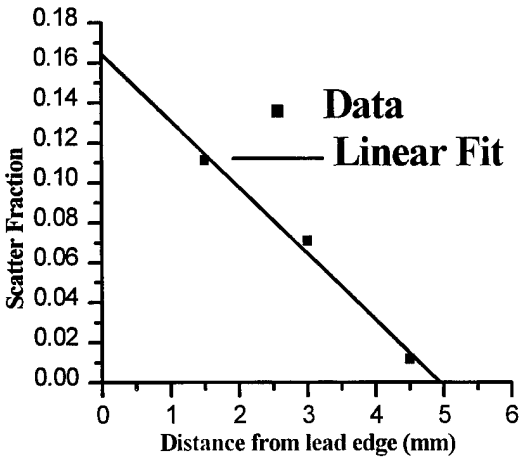

Figure 45. Scatter fraction versus distance from lead edge with parallel beam air gap.

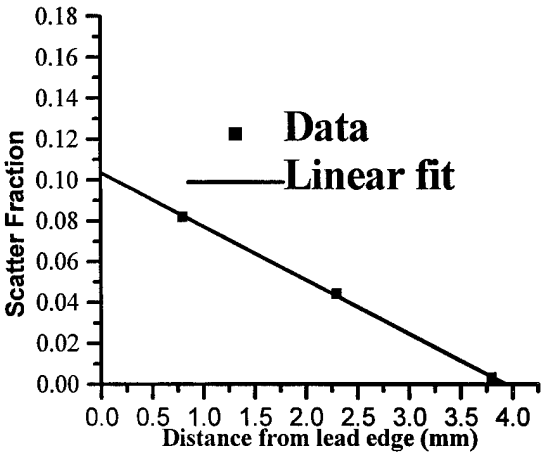

Figure 46. Scatter fraction versus distance from lead edge using lens.

case the measured value agrees quite well with the theoretical calculation. Because the scatter fractions in both cases are low, the contrast is almost the same.

Hole depth (mm)	Experiment		Theoretical	
	Lens	Parallel beam air gap	Lens	Parallel beam air gap
4	0.25±0.04	0.24±0.03	0.24	0.23
8	0.48±0.04	0.41±0.03	0.48	0.47

Table IV. Contrast values, measured for the 4 and 8 mm deep holes in the 1 cm thick Lucite phantom, for the lens and air gap. Theoretical calculations include the scatter fraction from figure 43 and 44.

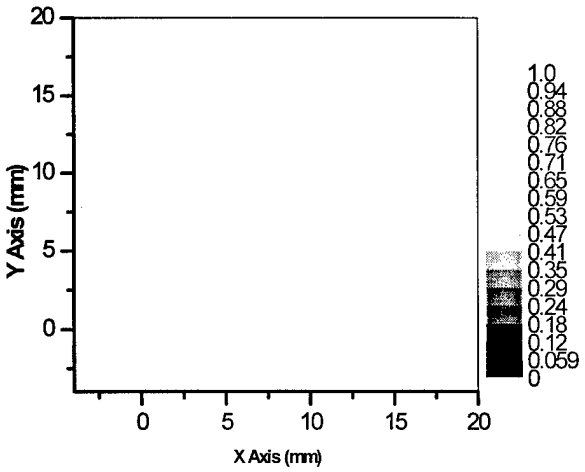

Figure 47. Image created from a Lucite phantom with different diameter and depth holes with a parallel beam air gap.

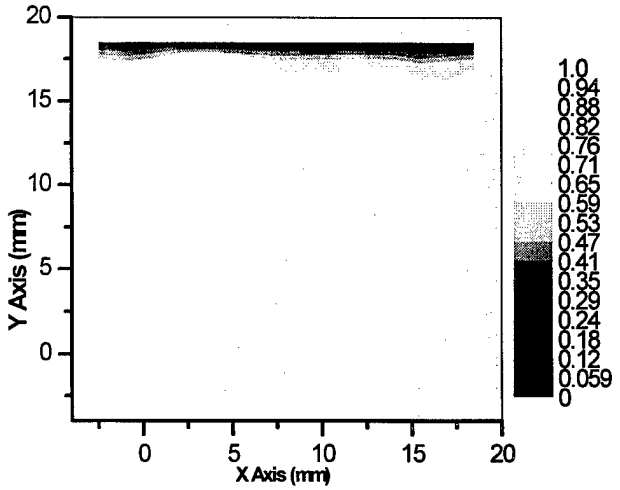

Figure 48. Image is created from a Lucite phantom with the lens.

2.H.2.b.2 Demagnification

The image in figure 48 is a smaller than that in figure 47, due to the demagnification produced by the focusing of the lens. The amount of demagnification can be calculated from the change in center-to-center distances between the holes, given in Table V. The average demagnification is 0.87, which is as expected since the image was taken approximately nine tenths of the way from the focal point of the lens. Demagnification of images is routinely performed in digital mammography systems by converting

the x rays to visible light and using lenses or fiber optics to decrease the size of the image. The manipulation of the x ray image directly may allow the use of direct digital detectors, which do not require a phosphor for conversion to visible light, and therefore can have higher resolution.

Hole center to center distance (mm)	Lens	Parallel beam air gap	Demagnification ratio
1-2	6.9	8.0	0.87
1-3	9.0	10.0	0.89
2-4	9.6	11.2	0.86
3-4	6.9	8.0	0.87

Table V. Change in distances due to demagnification. Average demagnification is 0.87±0.02.

3. Conclusion

A new, more physical model for describing profile defects in polycapillary x-ray optics at high energies for mammography has been developed. The simulation model M2, is physically plausible and works quite well in explaining the transmission spectra. It uses a clear technique for determining the parameters, which makes simulating the experimental results and designing lenses straightforward, easy and timesaving. According to the simulations, waviness and bending in the capillary channel profiles can be particularly harmful for high-energy photons because of the smaller critical angle at high energies. Roughness is not important in the simulation for borosilicate glass. It is expected that increasing the rigidity and straightness of the fiber and reducing the channel size to an optimum value can further increase the transmission. The spectra of transmission versus energy have been found to be a very sensitive tool in capillary quality analysis, and transmission versus source scan curve measurements can also provide significant information. Lead glass shows promise in allowing for shorter, higher transmission optics which will easier to manufacture.

The collimating lens with long focal distance of around 2 m has good transmission, uniformity and low exit divergence. The good agreement between the computer models and the single fiber data allowed accurate design and prediction of optic behavior. This contributed to the excellent performance of the lens, with a primary transmission of almost 45 % at 20 keV and nearly zero scatter transmission, and output divergence of only 1.2 mrad at 17 keV. Thus the lens can be used as a pre-patient optic to remove the variation of magnification and resolution of the image, and as a post-patient optic to reduce scatter transmission and enhance contrast at low patient dose. Using this lens in focusing mode with a parallel beam input, demagnification of the image was demonstrated. The lens also showed equal or better scatter rejection and contrast compared to a 34 cm air gap.

4. Key Research Accomplishments

- A new, more physical model for describing profile defects in polycapillary x-ray optics at high energies has been developed.
- A geometric simulation with two fiber defects, waviness and bending correction, agrees very well with experimental data for borosilicate fibers.

• The same geometry simulation with four fiber defects, waviness, bending, roughness and channel blockage, agrees very well with experimental data for leaded glass fibers.

• Measured and simulated single and bent borosilicated and lead glass fibers. The borosilicate glass had transmission around 70 % and the lead glass 45 % at 20 keV. The leaded glass has better scatter rejetion than borosilicate glass. Transmission agree well with simulations.

• Applied simulation from single fibers to a multifiber lens. This modeling is in good agreement with measurements. Therefore, characteristics from single fiber, simulations can be used to predict the behavior of a multifiber lens.

• Measured multifiber lens in collimating and focusing modes. The multifiber lens has good uniformity (non uniformity < 1.3 %) , high transmission (45 %), and low divergence (1.2 mrad). This makes it effective for use with a parallel beam input as a post-phantom demagnifying optic. The demagnification is 0.87 and agreed with prediction.

• The multifiber lens demontrated good scatter rejection, which occurs because of the tiny critical angles, and resulting selective reflection of on-axis rays by the glass walls.

5. Reportable Outcome

5.1 Manuscripts

Cari, Suparmi, S.D. Padiyar, W.M. Gibson, C.A. MacDonald, C. D. Alexander, M. K. Joy, C. H Russel, Z. W. Chen "Characterization of a Long Focal Length Polycapilary Optics for High Energy X rays", SPIE, Vol. 4144, 2000.

Suparmi, Cari, W.M. Gibson, C.A. MacDonald, "Development of Polycapillary X-Ray Optics for Scatter Rejection", SPIE, Vol. 4144, 2000.

Suparmi, Cari, Lei Wang, Hui Wang, W.M. Gibson, C.A. MacDonald, "Measurement and Analysis of Leaded Glass Polycapillary Optic Performance for Hard X Rays," to be submitted for Journal of Applied Physics.

5.2 Presentation

Cari, Suparmi, S.D. Padiyar, W.M. Gibson, C.A. MacDonald, C. D. Alexander, M. K. Joy, C. H Russel, Z. W. Chen ", Performance of a Long Focal Length Collimating Optic For Medical Imaging", Era of Hope Meeting, Atlanta, 2000.

5.3 Poster Presentation

Cari, Suparmi, S.D. Padiyar, W.M. Gibson, C.A. MacDonald, C. D. Alexander, M. K. Joy, C. H Russel, Z. W. Chen ", Performance of a Long Focal Length Collimating Optic For Medical Imaging", Era of Hope Meeting, Atlanta, 2000.

Cari, Suparmi, S.D. Padiyar, W.M. Gibson, C.A. MacDonald, C. D. Alexander, M. K. Joy, C. H Russel, Z. W. Chen "Characterization of a Long Focal Length Polycapilary Optics for High Energy X rays", SPIE, Vol. 4144, 2000.

Suparmi, Cari, W. M Gibson, C. A. MacDonald, " Measurement and Analysis Leaded Glass Polycapilary Optic for Mamography", Era of Hope Meeting, Atlanta, 2000.

6. References

1. ACS(American Cancer Society) "Cancer Facts And Figures," Atlanta, , GA: American Cancer Society, 1993.

2. P. Strax, "Detection Of Breast Cancer," Cancer 66,1336-1340, supplement,(1990).

3. M. A. Kumakhov, F. F. Komarov, "Multiple Reflection from Surface X-ray Optics", Physics Reports, 191,(5):p. 289-350,1990.

4. C. A. MacDonald, etc., "Quantitative measurements of the Performance of Capillary X-ray Optics "Multi-layer and Grazing Incidence X-Ray/EUV optics II, R. B. Hoover and A. Walker, eds., SPIE Proc. vol. 2011, 1993.

5. J. B. Ullrich, V. Kovantsev, C. A. MacDonald, "Measurements of Polycapillary X-ray Optics," Jour. Appl. Phys., 74(10),Nov. 15.,1993.

6. C.A. MacDonald, "Applications and Measurements of Polycapillary X-Ray Optics" Journal of X-ray Science and Technology, Special issue for the proceedings of the Monochromatic X-ray Workshop, 1993.

7. C.C. Abreu, D. G. Kruger, C.A. MacDonald, C.A. Mistretta, W.W. Peppler, Q. F. Xiao, Measurements of Capillary X-ray Optics with Potential for use in Mammographic Imaging, Medical Physics.

8. Q. F. Xiao, I. Y. Ponamarev, A. I. Kolomitsev and J.C. Kimball, "Numerical simulations for capillary-based x-ray optics," in X-Ray Detector Physics and Applications, R. B. Hoover, ed., SPIE 1992.

9. B. L. Henke, E. M. Gullikson, and J.C. Davis, Atomic Data and Nuclear Data Tables, 54 (2), p. 181, 1993.

10. J. C. Kimball, D. Bittel, "Surface roughness and scattering of glancing angle x-rays: Application to x-ray lenses", Jour. Appl. phys. 74 (2), 15 July 1993, pp. 877-883.

11. Lei Wang, B. K. Rath, W. M. Gibson, J.C. Kimball, C.A. MacDonald, "Performance Study of Polycapillary Optic Performance for Hard X rays," Journal of Applied Physics, 80 (7), pp.3628-3638, October 1, 1996.

12. B. K. Rath, D. C. Aloisi, D. H. Bilderback, N. Gao, W. M. Gibson, F. A. Hofmann, B. E. Homan, C. J. Jezewski, I. L. Klotzko, J. M. Mitchell, S. M. Owens, J. B. Ullrich, Lei Wang, G. M. Wells, Q. Xiao, C. A. MacDonald, "Effects of intense x-ray radiation on polycapillary fiber performance", in SPIE vol. 2519, X-Ray and Ultraviolet Sensors and Application, 1995.

13. B. K. Rath, Lei Wang, B. E. Homan, F. Hofmann, W. M. Gibson, C. A. MacDonald, "Measurements and analysis of Radiation effects in polycapillary x-ray optics", J. Appl. Phys.

14. F.R. Sugiro, SD. Padiyar, C.A. MacDonald, "Characterization of pre and post-patient X-Ray Polycapillary Optics for Mammography Imaging", SPIE, Vol. 4144, 2000

Brief Biography

Insvestigator name: Cari (no last name)

Doctoral student in Physic Department, The University at Albany, SUNY, NY 12222

Education

Doctoral student: University at Albany, PHD, expected in May 2001

Master in Physic: 5/91, The College at New Paltz, SUNY, New Palts, NY 12567

Undergraduate: 7/84, Physics Education, Institute of Teacher Training and Education, Semarang, Indonesia.

SPIE, Vol. 4144, 2000, Advances in Laboratory-Based X-Ray Sources and Optics,
Conference Chairs: Carolyn A. Macdonald, Univ. at Albany; Ali Khounsary, Argonne National Lab.

Characterization of a Long Focal Length Polycapillary Optic for High Energy X rays

Cari, Suparmi, Sushil D. Padiyar, W.M. Gibson, C.A. MacDonald
Center for X-ray Optics, University at Albany, SUNY, Albany, NY 12222
C. D. Alexander and M.K. Joy
Marshall Space Flight Center, NASA, Huntsville, Alabama 35812
C. H. Russell
Bede Scientific Inc, 14 Inverness Drive East Suite G-104, Englewood. CO 80112, USA
Z. W. Chen
X-Ray Optical Systems, Inc, Albany, NY 12203

ABSTRACT

Polycapillary fibers and a prototype collector for high energy x rays with a 2 m focal length have been fabricated and characterized. Measurements of a prototype collector, performed in collimating mode, show that the optic has high transmission, good uniformity, and small exit divergence. The transmission as a function of energy was analyzed using an extended single fiber geometrical optic simulation and the result shows that the simulation fits the data fairly well. Scatter transmission and contrast enhancement were measured in focussing mode using a parallel beam input.

1. INTRODUCTION

Polycapillary optics can be used to improve contrast and resolution in imaging. X rays are transported down the hollow capillary tubes by external reflection from smooth glass walls. A single polycapillary fiber is about 0.51 mm in diameter, and contains hundreds or thousands of hollow capillary tubes, 10 μm in diameter, as shown in figure 1. A multifiber lens was constructed by stringing 3039 flexible singe fibers through metal holding grids. The fibers at one end of the lens are parallel, and at the other end are pointed toward a common focal point, 2 m away. This means that this lens can be used to collimate or focus x rays. In collimating mode, the lens is used as a collimator to collect x rays from a point source at the focus and produce a nearly parallel beam. In focusing mode, the lens is used as a collector for parallel a beam input and produces a focused beam. The focused beam can be used to demagnify an image. This is of potential benefit for direct imaging with small area digital x-ray detectors.

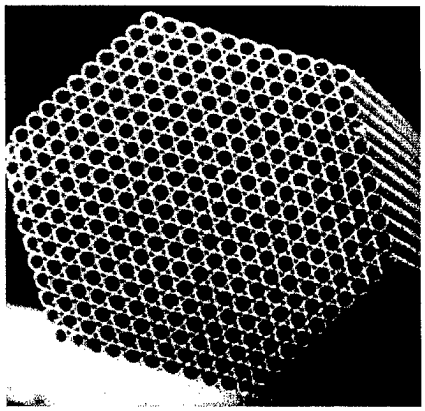

Figure 1. SEM of a single fiber. The diameter of the channels in this fiber is about 50μm. The fibers used in the experiment have open area of 70± 3 %, outer diameter of 0.51 mm and channel size of 10 μm, but similar structure.

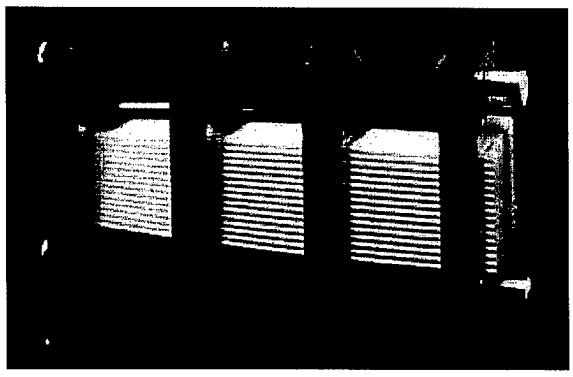

Figure 2. 3039 flexible fibers were strung through metal grids to produce the multifiber lens. This can be used as either a collimating or focusing lens. One end is parallel 30 mm x 30 mm. At the other end (29 mmx 29 mm) fibers are pointed at a focal point 2000 mm away.

2. BASIC PRINCIPLE OF POLYCAPILLARY OPTICS

The refractive index of glass for x rays can be written as

$$n = \sqrt{\frac{\varepsilon}{\varepsilon_0}} = 1 - \delta - i\beta \qquad (1)$$

where δ is the refractive index decrement and γ is proportional to absorption of the glass. Because the refractive index is less than one, x rays traveling from the air to glass will be totally externally reflected at small incidence angles. The critical angle for borosilicate glass is

$$\theta_c \cong \sqrt{\delta} \cong \frac{30\text{mrad}}{E(\text{keV})} \qquad (2)$$

where θ_c is in milliradians and E is the photon energy in keV. For example, the critical angle is 3.75 mrad for 8 keV photons and 0.375 mrad for 80 keV photons. When x-ray photons hit the glass walls of the channels at angles larger than critical angle, the photons will be absorbed. Because of the small critical angle, only primary x rays will be transmitted through the capillary channels to form an x-ray image, with near total scatter rejection of Compton scattered x rays.

3. STRAIGHT FIBER MEASUREMENTS

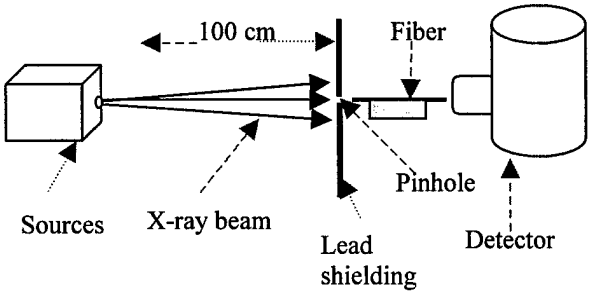

Figure 3. Experimental setup for single fiber measurement

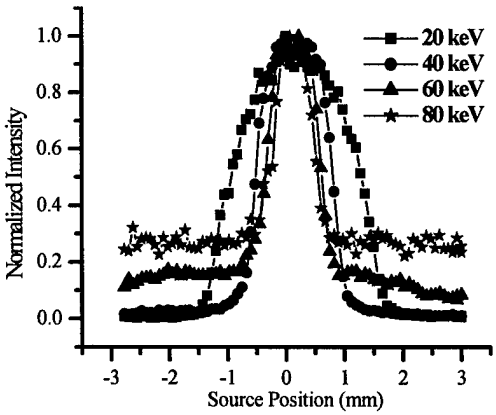

Figure 4. Measured source scan curve from 20 – 80 keV. The figure shows that there was no x-rays leakage.

The experimental setup for single fiber measurement is shown in figure 3. A microfocus source with a tungsten target and source spot size of 50 μm was used in the experiment. The source was mounted on two stages, which could be moved in two direction transverse to the beam, and also enclosed in a thick lead box to reduce scattered x-rays. The distance between the source and the fiber was about 100 cm to ensure incident angles less than critical angle up to energy 80 keV. A 200 μm pinhole was attached to thick lead shielding. The size of the pinhole is smaller than the diameter of the fiber which is about 0.5 mm to prevent scattering and leakage, to reduce the detector dead time and to keep the distance between the source and the fiber as small as possible, because of critical angle for high energies. The fractional open area of the fiber is 70 ± 3 %. The fiber was put on a finely machined groove in an aluminum plate mounted on two stages, which could be moved in two directions transverse to the beam. To ensure that source, pinhole, fiber and detector were aligned well, the transmission as a function of source location was measured, as shown in figure 4 for a fiber with length of 140 mm. The figure shows that there was not any x-ray leakage detected and the pinhole position was at the center of the fiber. Then the transmission of the fiber type used to construct the collimating lens were measured in the 10-80 keV energy range. Several fibers of different lengths were measured, three fibers from which are presented in figure 5.

3.1 Simulation Analysis

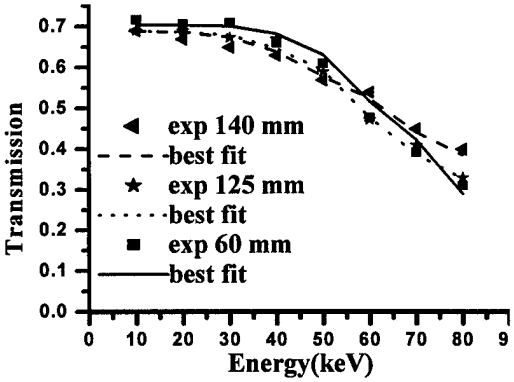

Figure 5. Transmission versus energy for single fibers with three different lengths. The lines are simulated data with waviness, w= 0.12 mrad, and roughness, z= 0.65 nm, but with different bending radius, R_{140}=210 m, R_{125}=105 m, R_{60}=48 m.

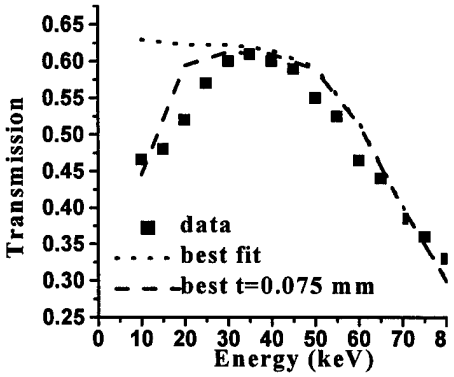

Figure 6. Simulated transmission compared with the experimental data for a defected fiber. Best fit is simulation with waviness, w=0.12 mrad, roughness, z=0.65 nm, bending radius, R=54 m, and glass layer thickness, t=75 μm.

The experimental data then was analyzed using a geometrical optic simulation to understand the performance of the fibers. The geometric algorithm is a two dimensional approximation. The geometric simulation includes three fiber defects: bending, waviness and roughness[1]. Bending is the deviation of the channel from an ideal straight path, approximated as uniform bending with a radius R. Waviness is local tilting of channel walls, parameterized by a standard deviation of tilt angles, w. Surface roughness is short wavelength surface variation, parameterized as an r.m.s. displacement z. The best fit simulation parameters were determined in the manner of reference 1. Using waviness from the source scan curve at 30 keV, roughness from source scan curve at 10 keV and adding a bending radius of 210 m, a fit was achieved across the whole spectrum. The simulated source scan curves with these three best fit simulation parameters for a 140 mm long fiber, compared with the experimental data, is shown in figure 5. Then the fitting processes were applied to two fibers with length of 125 mm and 60 mm. The simulated transmission spectra for these three fibers compared with experimental data are also shown in figure 5. Each simulation fits the experimental data well. Since the fibers are thin, a shorter fiber bends more and therefore transmits somewhat more poorly at high energies. All three lengths of fibers shown in figure 5 have good transmission up to energy 50 keV.

3.2 Defected Fiber

One of the fibers measured contained defects which caused the transmission to drop at low energies. The fiber was cut into two parts and their transmission was measured. One part with length of 60 mm also has low transmission at low energies, as shown in figure 6. It was suspected that the channels were blocked by glass layer of thickness t. The simulation, with waviness of 0.12 mrad and roughness 0.65 nm obtained in single fiber simulation previously, and adding the bending with radius of 54 m, fits the transmission spectrum data at only mid and high energies. Including a glass layer of thickness of 75 μm into the simulation, the simulated transmission fits the data quite well, as shown in figure 6. Therefore, the drop in transmission at low energies could be caused glass inclusion in the channels.[2]

3.3 Bent Fiber

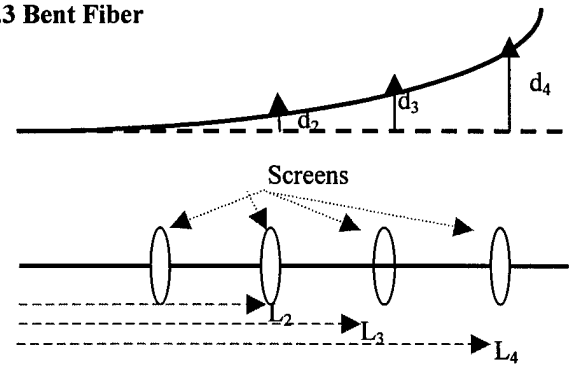

Figure 7. Sketch of fiber displacements for uniform bending measurements.

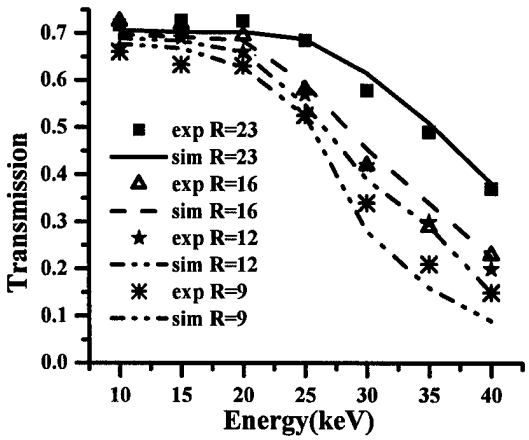

Figure 8. The simulated transmission compared with the experimental data for deliberately bend fiber. The lines are simulated data with waviness, w=0.12 mrad, and roughness, z= 0.65 nm, but with different bending radius, R.

In the straight fiber measurements, as shown in figure 3, the fiber was designed to be straight in the experimental setup. However, the fiber experienced unintentional bend because it was so thin. The bending radius was determined from the simulated transmission, fit to the experimental data. In the bending experiment, the fiber was inserted into four metal screens, as shown in figure 7. Initially, the fiber transmission was maximized and the transmission was measured and analyzed using the geometric simulation as for the straight fiber. The bending radius found from the simulation was called initial radius Ro and thus produced an initial fiber displacement from an ideal straight path. Then the fiber was bent intentionally by moving the actuator supporting the screen as in figure 7. The nearest screen to the input end of the fiber was fixed. Each screen displacement d_{move} was calculated so that the fiber bent in a uniform circle. The relation between the bending radius, R, and the screen displacement, d_i, is $R = L_i^2 / 2\, d_i$, where L_i is the length of the fiber from the input end to the i^{th} screen. Since in the initial measurement the fiber had been bent unintentionally with a radius R_o, and then displaced d_{move}, the total displacement of the fiber at the i^{th} screen is $d_i = (d_{oi} + d_{move})$. A fiber with length of 140 mm was measured in the bending setup. The initial position, the fiber assumed to be straight, was found from simulation to be unintentional bend with radius of 23 m. The simulation, with the bending radius calculated, as above, and using the waviness and roughness from straight fiber simulation (w=0.12 mrad and z=0.65 nm), fits the data quite well, as shown in figure 8. The good agreement between the computer models and the single fiber data allows accurate design and prediction of optic behavior.

4. MEASUREMENT AND ANALYSIS OF A LONG FOCAL LENGTH MULTIFIBER COLLIMATING LENS

A long focal length multifiber collimating lens with a length of 140 mm, input size of 29 mm X 29 mm and output size 30 mm x 30 mm was measured. The fibers were close-packed at the input end of the lens. The fiber packing fraction at the output end of the lens was 76.5%, therefore the total open area of the lens including the individual fiber open area of 70% was 54%. The lens was tested in both focussing and collimating mode. The focal length, transmission efficiency, uniformity and exit divergence were measured in collimating mode. Scatter rejection, contrast enhancement, and demagnification were demonstrated in focussing mode. In this mode the detector can be smaller than the object imaged.

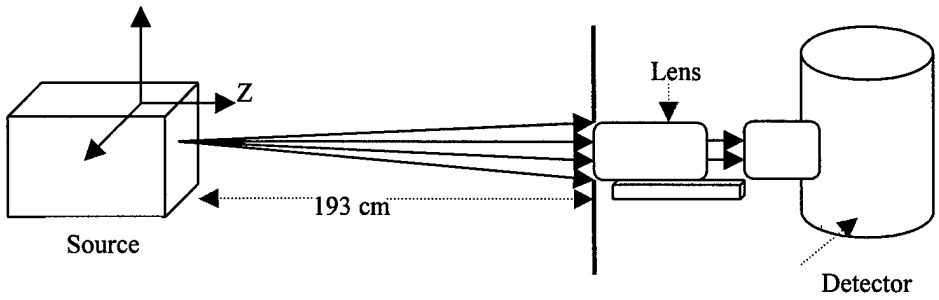

Figure 9. Experimental setup for transmission measurement of lens.

4.1 Experimental Setup

4.1.1 Collimating mode

The experimental setup to measure focal length, transmission efficiency, and uniformity of the lens, is shown in figure 9. The source was 193 cm from the input of the lens, the detector was 1 cm from the output of the lens.

4.1.1.1 Focal length

The focal length of the lens is the location at which the transmission is maximized. Transmission at different distances is shown in figure 10. The measured focal length of the lens was 192±1 cm. An image of the x-ray output of the lens with this source distance is shown in figure 11.

4.1.1.2 Transmission

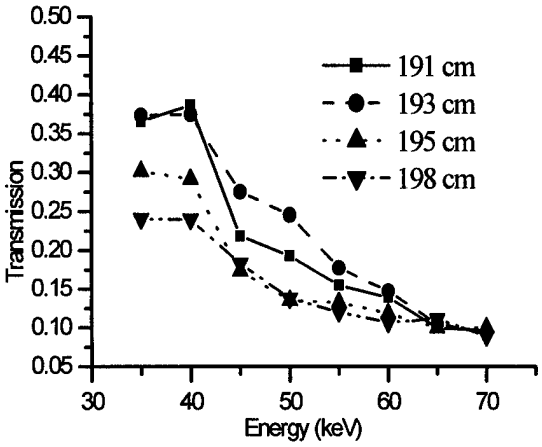

Figure 10. Transmission vs energy with difference source-lens distances. The transmission is maximized at 193 cm.

The transmission as a function of energy was measured. To explain the experimental result, a geometric simulation for single fibers was extended to simulate the lens.
The bending radius of fibers at each location in the lens was calculated using a simple geometric formula. The number of fibers with each bending radius was determined. Putting together all three simulation parameters, waviness and roughness from the single fiber simulation, and bending radius calculated at each fiber location in the lens, the simulated transmission spectrum was obtained. The simulated transmission spectrum for the whole lens is the average transmission spectra of all the locations normalized with the total fractional open area of the lens. The simulated transmission spectrum compared to experimental data is shown in figure 12. The simulated transmission fits the experimental data better at higher energies than lower ones since the channels of some fibers in the lens were blocked by glass inclusion.[1,2] The lens has good transmission up to 40 keV, and therefore seems promising for low and mid range energy applications, such as mammography, astronomy and angiography.

4.1.1.3 Uniformity

Figures 13 and 14 are two-dimensional output scans of the lens at 45 keV and and 60 keV, respectively. These were recorded by moving a 5 mm diameter aperture in two directions perpendicular to the lens axis,

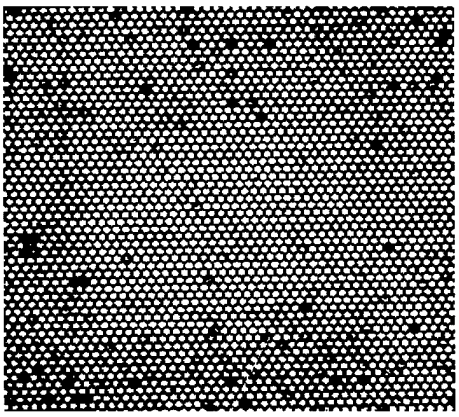

Figure 11. Photograph of the output of the lens with the source at the focal distance.

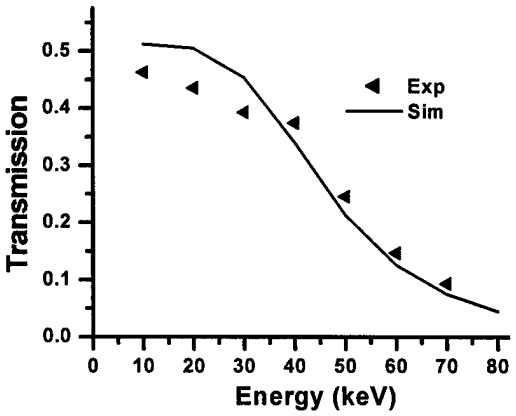

Figure 12. Simulated transmission compared to experimental data for the long focal length collimating lens.

with source, lens, and detector fixed. The higher the energy, the lower the transmission of the outer edges of the lens. This is expected, because of smaller critical angle at higher energies.

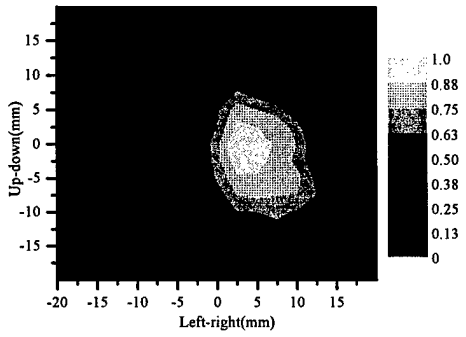

Figure 13. Output intensity from two dimensional scan of lens output at 45 keV

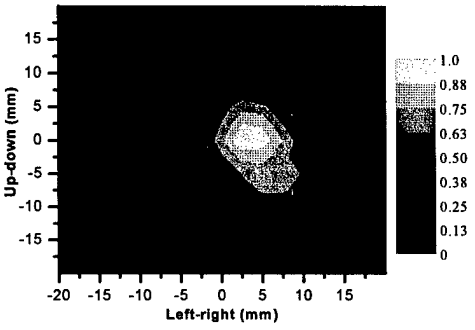

Figure 14. Output intensity from two dimensional scan at 60 keV

4.1.1.4 Exit Divergence

Measurements of the exit divergence of the collimating lens were performed at 17.5 keV with a Mo source and NaI detector as shown in figure 15. The total divergence was measured by rocking a (100) silicon wafer in the beam, using the (400) Bragg diffraction, without any aperture at the exit of the lens. The results of the total exit divergence are shown in Figure 16. Local divergence was measured with a 9.5 mm diameter aperture at upper left (ul), upper center (uc), upper right (ur), center left (cl), center (c), center right (cr), bottom left (bl), bottom center (bc), and bottom right (br) on the exit of the lens. The results of the local divergence are shown in table I. In general, the divergence is low, which requires that the fibers are very parallel at exit. Some areas (uc and bc) had poor alignment, and the fibers were replaced. The average local divergence is in agreement with the value of the total divergence, 1.2 mrad.

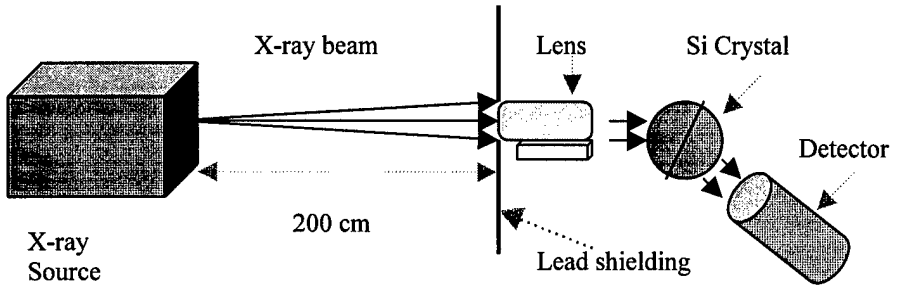

Figure 15. Experimental setup for exit divergence of lens

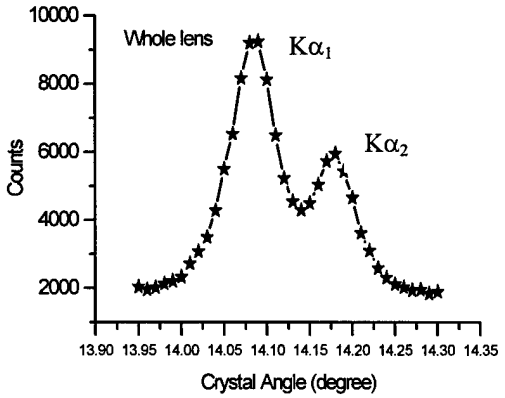

Figure 16. Total divergence, rocking curve. The first peak is diffraction of the Mo $K\alpha_1$ and the second the Mo $K\alpha_2$ characteristic lines. The FWHM of the first peak was 1.2 mrad.

Local divergence		
UL=1.2	UC=1.5	UR=1.0
CL=0.9	C=0.9	CR=1.1
BL=1.2	BC=1.5	BR=1.3

Table I. Local exit divergence, in mrad at the nine aperture locations.

4.2 Focusing Mode

In focusing mode, the focusing end of the lens faced the detector, thus the lens acted as a collector to the incoming parallel beam. Testing of this lens was performed at the Stray Light Facility (SLF) at Marshall Space Flight Center (MSFC) in Huntsville, Alabama where a very parallel source beam was available. X rays from a copper source enter a vacuum tube 100 m in the length and exit into the testing area. Measurements at the stray light facility are complicated by the low count rate of the photons because of the huge source-to-detector distance. Data was collected over a 10 keV energy window 15-25 keV, to increase the count rate.

4.2.1 Contrast and scatter rejection measurements

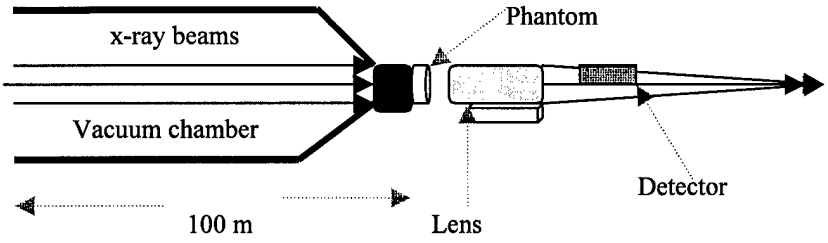

Figure 17. Experimental setup for contrast and scatter measurement.

Contrast is defined as the log of the ratio of the intensity through the area of interest to the intensity of the neighboring background.

$$C = \log (I_p / I_{bg}) \qquad (3)$$

where I_p is the intensity through object of interest, and I_{bg} is the neighboring

background intensity. Contrast is reduced by the presence of scattered x rays which emerge at all angles from the patient and form a background fog. Contrast with scatter is

$$C_s = \ln(I_p+I_s)/(I_p+I_s), \quad (4)$$

where I_s is the intensity of the scatter.
Scatter fraction is defined as

$$SF = [I_s/(I_s+I_p)] \quad (5)$$

Scatter can be removed from the beam by either an air gap or a polycapillary optic. The introduction of an air gap causes the intensity of the isotropic scatter radiation to drop faster than the forward-directed primary beam. For conventional sources, air gaps hurt resolution because the geometric blur from the finite source increases with object to detector distance. Here, the parallel beam has very low geometric blur. Alternatively, the scatter radiation, which emerges from the phantom at high angles, can be absorbed by the glass walls of the polycapillary optic, as shown in figure 18. Only the forward-directed primary beam is carried down the channels.

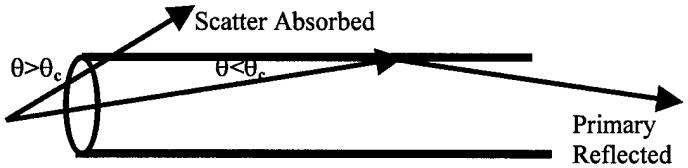

Figure 18. Mechanism photons of x rays through the glass wall.

Contrast and scatter fraction measurements were performed in focusing mode as shown in figure 17 with a detector-lens distance of 20 cm. The scatter fraction was measured by placing a lead block in the beam and measuring the scattered fog intensity behind the block due to a 2.5 cm thick Lucite phantom. By scanning the detector, the scatter intensity behind the block can be measured as shown in figure 19 and 20. The polycapillary lens is even better than parallel beam air gap at removing the scatter. To measure contrast, a 1 cm thick Lucite phantom with holes of different diameter and depth was attached on the output of the vacuum chamber. Two cases were measured. In the first, air gap case, the lens was removed and detector was placed 34 cm from the phantom. Because the air gap removes most of the scatter, the contrast is good. In the second case, the lens was put in place and detector inserted 20 cm from the lens. Distance between the phantom and the lens was 3 cm. The output was scanned using a small (3 mm x 3 mm) detector. The intensity was measured for 60 seconds at each location, and the data assembled as an image, as shown in figures 21 and 22. The contrast was determined from the measured intensity behind and near each hole and is shown in table II. Contrast was also calculated from the theoretical attenuation in the plastic, corrected for the known scatter fractions. In each case the measured value agrees quite well with the theoretical calculation. Because the scatter fractions in both cases are low, the contrast is almost the same.

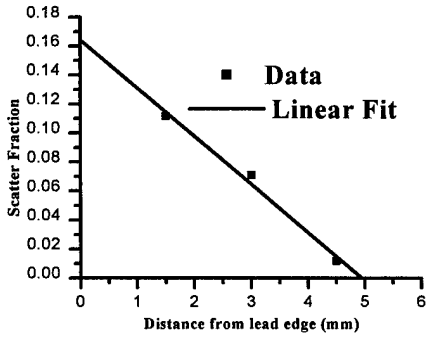

Figure 19. Scatter fraction versus distance from lead edge with parallel beam air gap.

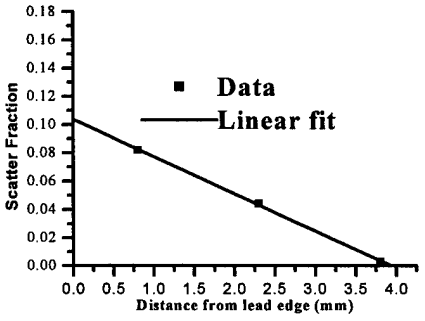

Figure 20. Scatter fraction versus distance from lead edge using lens.

Hole depth (mm)	Experiment		Theoretical	
	Lens	Parallel beam air gap	Lens	Parallel beam air gap
4	0.25±0.04	0.24±0.03	0.24	0.23
8	0.48±0.04	0.41±0.03	0.48	0.47

Table II. Contrast values, measured for the 4 and 8 mm deep holes in the 1 cm thick Lucite phantom, for the lens and air gap. Theoretical calculations include the scatter fraction from figure 19 and 20.

4.2.2 Demagnification

The image in figure 22 is a smaller than that in figure 21, due to the demagnification produced by the focusing of the lens. The amount of demagnification can be calculated from the change in center-to-center distances between the holes, given in Table III. The average demagnification is 0.87, which is as expected since the image was taken approximately nine tenths of the way from the focal point of the lens. Demagnification of images is routinely performed in digital mammography systems by converting the x- ray to visible light and using lenses or fiber optics to decrease the size of the image. The manipulation of the x-ray image directly may allow the use of direct digital detectors, which do not require a phosphor and conversion to visible light, and therefore can have higher resolution.

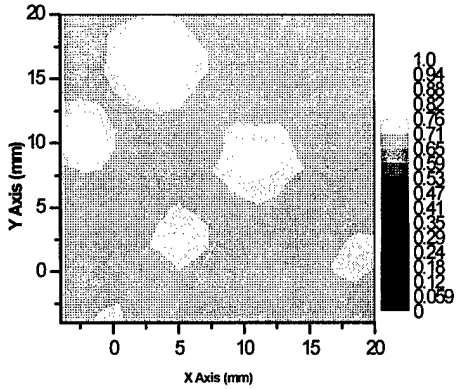

Figure 21. Image created from a Lucite phantom with different diameter and depth holes with a parallel beam air gap.

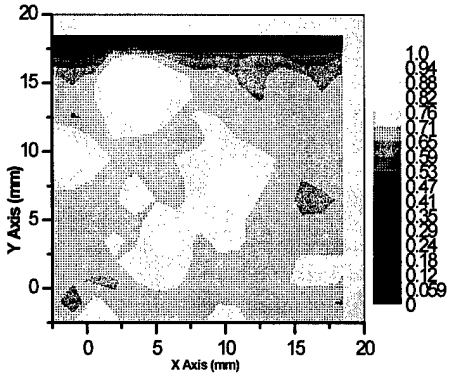

Figure 22. Image is created from a Lucite phantom with the lens.

Hole center to center distance (mm)	Lens	Parallel beam air gap	Demagnification ratio
1-2	6.9	8.0	0.87
1-3	9.0	10.0	0.89
2-4	9.6	11.2	0.86
3-4	6.9	8.0	0.87

Table III. Change in distances due to demagnification. Average demagnification is 0.87±0.02.

5. CONCLUSION

The good agreement between the computer models and the single fiber data allowed accurate design and prediction of optic behavior. This contributed to the excellent performance of the lens, with a transmission of > 38 % at 10-40 keV, and output divergence of only 1.2 mrad at 17 keV. Using this lens in focusing mode with a parallel beam input, demagnification of the image was demonstrated. The lens also showed equal or better scatter rejection and contrast compared to a 34 cm air gap.

6. ACKNOWLEDGEMENT

The authors gratefully acknowledge the ideas, discussion and assistance from Hui Wang and Lei Wang. This work was supported by the Department of Army Breast Cancer Research Project and The National Institutes of Health.

7. References

1. Suparmi, Cari, W.M. Gibson, C.A. Macdonald, "Development of Polycapillary X-Ray Optics for Scatter Rejection", SPIE', Vol 4144, 2000.
2. F.R. Sugiro, S.D. Padiyar, C.A. Macdonald, "Characterization of pre-and post-patient X-ray Polycapillary Optics for Mammography Imaging", SPIE, Vol 4144, 2000.
3. J.B Ullrich, V. Kovantsev, C.A. MacDonald, "Measurements of Polycapillary X-Ray Optics", Jour. Appl. Phys., 74 (10), Nov. 15, 1993, pp. 5933-5939.
4. C.C. Abreu, D.G. Kruger, C.A. MacDonald, C.A. Mistretta, W.W. Peppler, Q. Xiao, "Measurements of Capillary X-Ray Optics with Potential for Use in Mammographic Imaging", Medical Physics, 1995, Vol. 22, Issue 11, pp. 1793-1801.
5. David G. Kruger, Carmen C. Abreu, Eric G. Hendee, Armen Kocharian, Walter W. Pepler, and Charles A. Mistreta, Imaging Characteristics of X-ray Capillary Optics in Digital Mammography, Medical Physics, vol 23, no.2, 1996
6. Kardiawarman, Multifiber Polycapillary -Based X-ray Collimating Lens For X-Ray Diffraction, Thesis, Department of Physics, University at Albany, 1995,pp. 30-35
7. C.C. Abreu and C.A. MacDonald, "Beam Collimating, Focusing, Filtering and Imaging with Polycapillary X-ray and Neutron Optics," Physica Medica, vol. XIII, N.3, 1997, pp. 79-89.
8. C.H. Russell, W. M. Gibson, M. V. Gubarev, F. A. Hofmann, M. K. Joy, C. A. MacDonald, Lei Wang, Qi-Fan Xiao, R. Youngman, "Application of Polycapillary Optics for Hard X-Ray Astronomy", in Grazing Incidence and Multilayer X-ray Optical Systems, R.B. Hoover and A. Walker II, eds., SPIE vol. 3113, pp. 369-377, 1997.
9. Lei Wang, C. A. MacDonald, "Measurement of Capillary Optic Performance for Hard X rays", in X-Ray and Ultraviolet Sensors and Applications, SPIE vol. 2519, 1995, pp. 219-223.
10. Lei Wang, B.K. Rath, W.M. Gibson, J.C. Kimball, C.A. MacDonald, "Performance Study of Polycapillary Optic Performance for Hard X rays," Journal of Applied Physics, 80 (7), pp.3628-3638, October 1, 1996.